

# Automatic Foreground Extraction using Multi-Agent Consensus Equilibrium

Xiran Wang, *Student Member, IEEE*, Jason Juang and Stanley H. Chan, *Senior Member, IEEE*

**Abstract**—While foreground extraction is fundamental to virtual reality systems and has been studied for decades, majority of the professional softwares today still rely substantially on human interventions, e.g., providing trimaps or labeling key frames. This is not only time consuming, but is also sensitive to human error. In this paper, we present a fully automatic foreground extraction algorithm which does not require any trimap or scribble. Our solution is based on a newly developed concept called the Multi-Agent Consensus Equilibrium (MACE), a framework which allows us to integrate multiple sources of expertise to produce an overall superior result. The MACE framework consists of three agents: (1) A new dual layer closed-form matting agent to estimate the foreground mask using the color image and a background image; (2) A background probability estimator using color difference and object segmentation; (3) A total variation minimization agent to control the smoothness of the foreground masks. We show how these agents are constructed, and how their interactions lead to better performance. We evaluate the performance of the proposed algorithm by comparing to several state-of-the-art methods. On the real datasets we tested, our results show less error compared to the other methods.

**Index Terms**—Foreground extraction, alpha matting, video matting, Multi-Agent Consensus Equilibrium, background subtraction

## 1 INTRODUCTION

### 1.1 Motivation

The proliferation of virtual reality displays and rendering technology over the past decade is rapidly changing the landscape of cinematography [1]–[4]. From the traditional motion pictures to the recent 3D animation, it is safe to argue that the next wave in the film-making industry is immersive experience, e.g., head-mounted virtual reality displays. In order to offer sufficient content for these displays, data has to be acquired in special ways, e.g., using 360-degree volumetric imagers [5]. Typically, such videos are high-definition  $1920 \times 1080$ , full frame rate at 60 fps, and are captured using as many as 100 cameras simultaneously. This is an enormous amount of data: A five-minute video sequence using the above configuration is already equal to more than one million images. Efficient image processing of these images is therefore critical.

The subject of this paper is the classical foreground extraction [6]–[8] in the image processing pipeline of a virtual reality system. Foreground extraction is a well-established computer vision technique which extracts the foreground object from the background. Our main contribution is a *fully automatic* approach which does not require any human intervention. This makes a fundamental difference with the mainstream semi-supervised methods such as alpha matting which require scribbles or trimaps [9]–[13].

The motivation of developing a fully-automatic solution is two-fold. First, from a man-power perspective, drawing trimaps by human operators is infeasible for large volume of images. While commercial softwares can speed up the

process, in many cases professional artists still need to create trimaps for individual frames, or at least for the so-called “key-frames”. Second, from an image quality perspective, while trimap generation algorithms exist [14]–[17], many of them generate false labels. For certain low-resolution surveillance applications this may not be a problem, yet for filming applications these false labels will make the object masks unacceptable.

### 1.2 Scope and Assumptions

Foreground extraction is one of the mostly studied topics in computer vision. Given the sheer amount of foreground extraction algorithms in the literature, it would be over-optimistic or even unrealistic to claim uniformly better performance over all existing methods. To put our method into a proper context, we focus on conditions that can be met in a filming environment.

**Assumption 1. Plate Image Available.** First, we assume that a background image, called the *plate* image, is available. Obtaining a plate image is feasible in most filming environments, where the camera can shoot the background before an object enters the scene or after the object leaves the scene. The plate image does not need to be completely static. Minor motions and changes are allowed, e.g., movement of trees, illumination change due to the sun, or exposure change due to the auto-exposure function of a camera.

**Assumption 2. Focus on Major Boundaries.** Second, we focus on recovering *major* object boundaries, because these have strong influence to the quality of the images shown on virtual reality displays. Fine details such as hair are important but they are beyond the scope of this paper. While we still make comparisons to methods on [alphamatting.com](http://alphamatting.com), our goal is not to aim for extremely high precision boundaries. We also do not consider transparent objects in this paper.

X. Wang and S. Chan are with the School of Electrical and Computer Engineering, Purdue University, West Lafayette, IN 47907, USA. Email: {wang470, stanchan}@purdue.edu.

J. Juang is with HypeVR Inc., San Diego, CA 92108, USA. Email: jason@hypevr.com

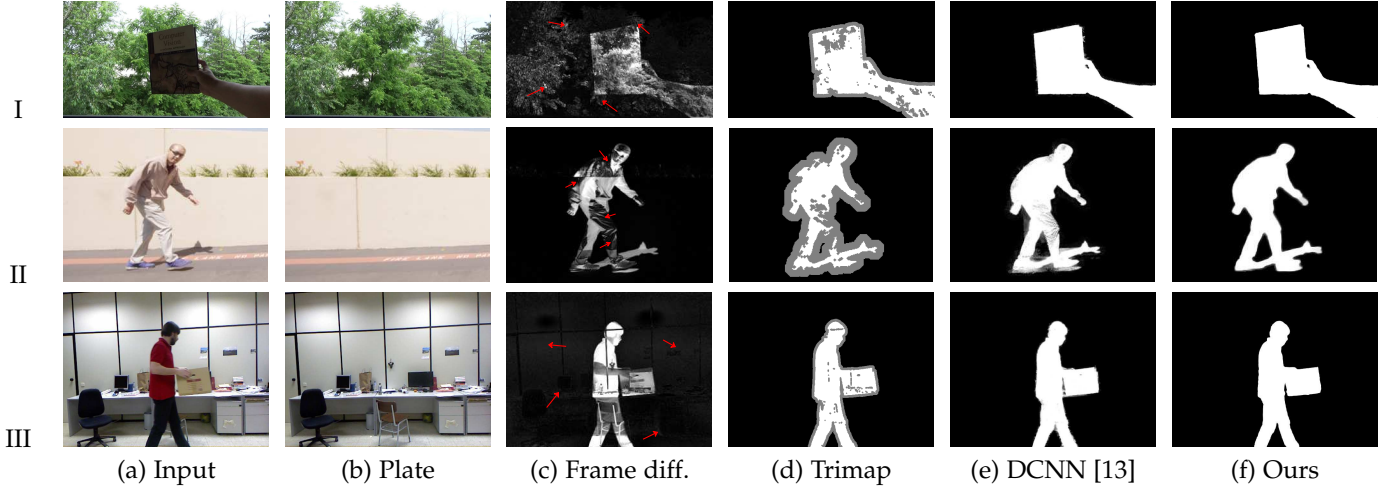


Fig. 1. Three common issues of automatic foreground extraction. Case I: Vibrating background. Notice the small vibration of the leaves in the background. Case II: Similar foreground / background color. Notice the missing parts of the body of the man, and the excessive large uncertainty region of the trimap. Case III: Auto-exposure. Notice the false alarm in the background of the frame difference map. We compare our method with DCNN [13], a semi-supervised alpha matting method using the generated trimaps. The video data of Case III is from [18].

### 1.3 Challenges

Readers at this point may argue that the plate assumption is too strong: If the plate is available, it seems that a standard frame difference with some morphographic operation (e.g., erosion / dilation) would be enough to provide a trimap, and thus a sufficiently powerful alpha matting algorithm would work. However, except for synthetic videos, plate images are never perfect. Below are three of the most common issues of a plate image.

- **Background vibration.** While we assume that the plate does not contain large moving objects, small vibration of the background generally exists. Figure 1 Case I shows an example where the background tree vibrates.
- **Color similarity.** When foreground color is very similar to the background color, the trimap generated will have false alarms and misses. Figure 1 Case II shows an example where the cloth of the man has a similar color to the background wall.
- **Auto-exposure.** If auto-exposure is used, the background intensity will change over time. Figure 1 Case III shows an example where the background cabinet becomes dimmer when the man leaves the room.

As one can see in these examples, error in frame difference can be easily translated to false alarms and misses in the trimap. While we can increase the uncertainty region of the trimap to rely more on the color constancy model of the alpha matting, in general alpha matting performs worse when the uncertainty region grows. We have also tried more advanced background estimation algorithms, e.g., [19] in the OpenCV library. However, the results are similar or sometimes even worse.

### 1.4 Related Work

To the best of our knowledge, none of the existing *fully-automatic* foreground extraction methods can simultaneously address all the above issues while generating high quality foreground masks. Below we highlight some major prior work and comment on their limitations.

- **Alpha Matting.** The mostly related approach to our work is alpha matting. Alpha matting typically formulates the problem as minimizing certain energy function associated with the foreground and background color. Examples include Poisson matting [21], closed-form matting [20], shared matting [22], Bayesian matting [23], and robust matting [24]. More recently, deep neural network based approaches become popular, e.g., deep matting [25] and DCNN matting [13]. Alpha matting algorithms require *error-free* trimaps. However, creating a error-free trimap could be as time consuming as solving the original alpha matting problem.
- **Video Matting.** Video matting algorithms extend alpha matting by considering the temporal dimension [26]–[28]. The temporal consistency is handled by introducing constraints or regularization functions. Trimaps are still needed for these algorithms, which could become intractable when the video is long. Alternative methods such as [29]–[31] identify key frames of the video and propagate the user labeled alpha mattes to adjacent frames. However, the propagation is often error-prone especially in the case of occlusion. As a result, users need to interrupt the process by cleaning up the alpha mattes, and re-iterate the algorithm multiple times to obtain a final result.
- **Background Subtraction.** Background subtraction methods range from the simple frame difference method to the more sophisticated mixture models [32]. These methods also include classical video segmentation methods, e.g., using saliency [33], [34]. Most background subtraction methods are used to track objects instead of extracting the alpha mattes. They are fully-automated and are real time, but the foreground masks generated are usually of low quality.
- **Trimap Generation.** In the absence of trimaps, there are multi-stage methods to first create the trimap and then perform alpha matting [14]. However, these methods still require initial segmentations using e.g., GrabCut [6]. Other methods [35], [36] require additional sensor data, e.g., depth measurements, which are not always available.

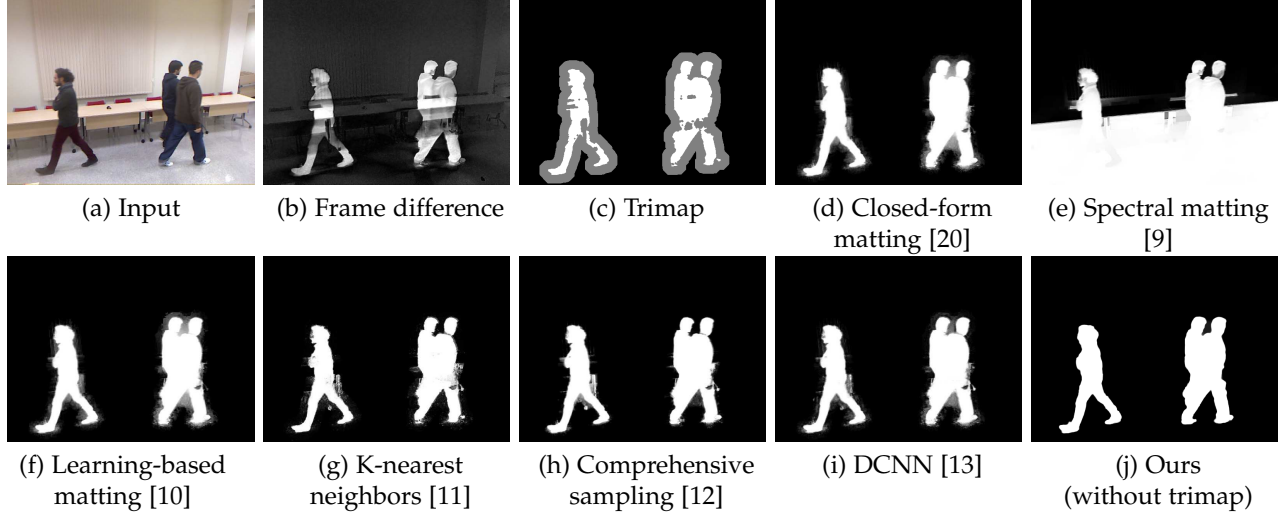


Fig. 2. Comparison with existing alpha-matting algorithms on real images with a frame-difference based trimap. (a) Input image. (b) Frame difference. (c) Trimap generated by morphographic operation (dilation / erosion) of the binary mask. (d) - (i) Alpha matting algorithms available on [alphamatting.com](http://alphamatting.com). (j) Proposed method. This sequence is from the dataset of [18].

Figure 2 illustrates the performance of various alpha matting algorithms applied to a multi-object-moving scene. In this example, we use frame difference to construct a trimap and then apply various alpha matting algorithms to estimate the alpha matte. As shown, the proposed method produces the most reliable foreground masks. More discussions of the experiment can be found in the Section 4.

## 1.5 Contributions

This paper contributes to the foreground extraction problem by offering two new ideas:

- **Multi-Agent Consensus Equilibrium (MACE).** We introduce a framework called the multi-agent consensus equilibrium (MACE). MACE is an information fusion framework that allows us to integrate multiple sources of experts to generate better overall results. Originally developed from the Plug-and-Play ADMM [36]–[38], MACE offers significantly greater flexibility for non-optimization based operations. We demonstrate, for the first time, how MACE can be used to solve a foreground extraction problem, something beyond the classical image restoration problems, e.g., denoising and deblurring.
- **Designing Agents for MACE.** Under the MACE framework, we need to define appropriate agents. In this paper, we present three customized agents for the foreground extraction task: (1) A new dual-layer alpha matting agent to estimate the foreground mask; (2) A background probability estimator to estimate the background; (3) A total variation minimization operator to smooth out the results. We show the effectiveness of these agents in solving the foreground extraction problem.

In order to explain all the essential concepts, we organize the paper in a way that the general framework and the specific components are addressed in two different sections. In Section 2 we describe the MACE framework. We will discuss its derivation, the intuition, and the algorithm. Then in Section 3 we go deep into the details of each component of the MACE framework that are specific to foreground extraction. Experimental results are presented in Section 4.

## 2 MULTI-AGENT CONSENSUS EQUILIBRIUM

The main ingredient of the proposed method is the concept of Multi-Agent Consensus Equilibrium (MACE), recently developed by Buzzard, Chan, Sreehari and Bouman [39]. In this section, we describe the key components of MACE and provide simplified proofs to discuss why MACE work. We also show how MACE is linked to the classical ADMM algorithm in the optimization literature.

### 2.1 ADMM

The starting point of MACE is the alternating direction method of multiplier (ADMM) algorithm [40]. The ADMM algorithm is a method commonly used to solve a constrained minimization:

$$\underset{\mathbf{x}_1, \mathbf{x}_2}{\text{minimize}} \quad f_1(\mathbf{x}_1) + f_2(\mathbf{x}_2), \quad \text{subject to} \quad \mathbf{x}_1 = \mathbf{x}_2, \quad (1)$$

where  $\mathbf{x}_i \in \mathbb{R}^n$ , and  $f_i : \mathbb{R}^n \rightarrow \mathbb{R}$  are mappings, typically a forward model describing the image formation process and a prior distribution of the latent image. ADMM solves the problem by solving a sequence of subproblems as follows:

$$\mathbf{x}_1^{(k+1)} = \underset{\mathbf{v} \in \mathbb{R}^n}{\text{argmin}} \quad f_1(\mathbf{v}) + \frac{\rho}{2} \|\mathbf{v} - (\mathbf{x}_2^{(k)} - \mathbf{u}^{(k)})\|^2, \quad (2a)$$

$$\mathbf{x}_2^{(k+1)} = \underset{\mathbf{v} \in \mathbb{R}^n}{\text{argmin}} \quad f_2(\mathbf{v}) + \frac{\rho}{2} \|\mathbf{v} - (\mathbf{x}_1^{(k+1)} + \mathbf{u}^{(k)})\|^2, \quad (2b)$$

$$\mathbf{u}^{(k+1)} = \mathbf{u}^{(k)} + (\mathbf{x}_1^{(k+1)} - \mathbf{x}_2^{(k+1)}). \quad (2c)$$

In the last equation (2c), the vector  $\mathbf{u}^{(k)} \in \mathbb{R}^n$  is the Lagrange multiplier associated with the constraint. Under mild conditions, e.g., when  $f_1$  and  $f_2$  are convex, close, and proper, global convergence of the algorithm can be proved [37]. Recent studies show that ADMM converges even for some non-convex functions [38].

When  $f_1$  and  $f_2$  are convex, the minimizations in (2a) and (2b) are known as the proximal maps of  $f_1$  and  $f_2$ , respectively [41]. If we define the proximal maps as

$$F_i(\mathbf{z}) = \underset{\mathbf{v} \in \mathbb{R}^n}{\text{argmin}} \quad f_i(\mathbf{v}) + \frac{\rho}{2} \|\mathbf{v} - \mathbf{z}\|^2, \quad (3)$$

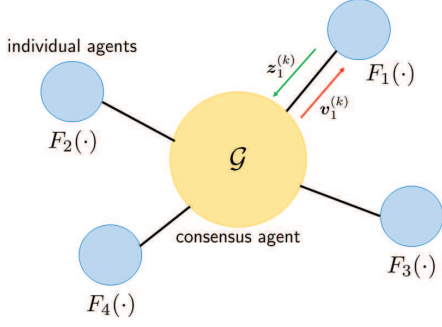


Fig. 3. Conceptual illustration of MACE. There are two sets of agents: The individual agents, and the consensus agent. The individual agents perform their own tasks and send the signal  $z_i^{(k)}$  to the consensus agent, whereas the consensus agent gathers the information and broadcast the feedback signal  $v_i^{(k)}$ .

then it is not difficult to see that at the optimal point, (2a) and (2b) become

$$F_1(\mathbf{x}^* - \mathbf{u}^*) = \mathbf{x}^*, \quad (4a)$$

$$F_2(\mathbf{x}^* + \mathbf{u}^*) = \mathbf{x}^*, \quad (4b)$$

where  $(\mathbf{x}^*, \mathbf{u}^*)$  are the solutions to the original constrained optimization in (1). (4a) and (4b) shows that the solution  $(\mathbf{x}^*, \mathbf{u}^*)$  can now be considered as a fixed point of the system of equations.

Rewriting (2a)-(2c) in terms of (4a) and (4b) allows us to consider agents  $F_i$  that are not necessarily proximal maps, i.e.,  $f_1$  is not convex or  $F_1$  may not be expressible as optimizations. One example is to use an off-the-shelf image denoiser for  $F_2$ , e.g., BM3D, non-local means, or neural network denoisers. Such algorithm is known as the Plug-and-Play ADMM [37], [38], [42] (and variations thereafter [39], [43]).

## 2.2 MACE and Intuition

Multi-agent consensus equilibrium (MACE) generalizes the above ADMM formulation. Instead of minimizing a sum of two functions, MACE minimizes a sum of  $N$  functions  $f_1, \dots, f_N$ :

$$\underset{\mathbf{x}_1, \dots, \mathbf{x}_N}{\text{minimize}} \quad \sum_{i=1}^N f_i(\mathbf{x}_i), \quad \mathbf{x}_1 = \dots = \mathbf{x}_N. \quad (5)$$

In this case, the equations in (4a)-(4b) are generalized to

$$\begin{aligned} F_i(\mathbf{x}^* + \mathbf{u}_i^*) &= \mathbf{x}^*, \quad \text{for } i = 1, \dots, N \\ \sum_{i=1}^N \mathbf{u}_i^* &= 0. \end{aligned} \quad (6)$$

What does (6) buy us? Intuitively, (6) suggests that in a system containing  $N$  agents  $F_1, \dots, F_N$ , each agent creates a tension  $\mathbf{u}_i^* \in \mathbb{R}^n$ . For example, if  $F_1$  is an inversion step whereas  $F_2$  is a denoising step, then  $F_1$  will not agree with  $F_2$  because  $F_1$  tends to recover details but  $F_2$  tends to smooth out details. However, when putting into zero-sum dynamical system, the agents  $F_1, \dots, F_N$  have to reach an equilibrium state where the sum of the tension is zero. This also explains the name ‘‘consensus equilibrium’’, as the algorithm is seeking a consensus among all the agents. A pictorial illustration of the MACE concept is shown in Figure 3.

## 2.3 Algorithm to Achieve Equilibrium

How does the equilibrium solution look like? The following theorem, shown in [39], provides a way to connect the equilibrium condition to a fixed point of a dynamical system.

**Theorem 1** (MACE solution). *Let  $\mathbf{u}^* \stackrel{\text{def}}{=} [\mathbf{u}_1^*; \dots; \mathbf{u}_N^*]$ . The consensus equilibrium  $(\mathbf{x}^*, \mathbf{u}^*)$  is a solution to the MACE equation (6) if and only if the points  $\mathbf{v}_i^* \stackrel{\text{def}}{=} \mathbf{x}^* + \mathbf{u}_i^*$  satisfy*

$$\frac{1}{N} \sum_{i=1}^N \mathbf{v}_i^* = \mathbf{x}^* \quad (7)$$

$$(2\mathcal{G} - \mathcal{I})(2\mathcal{F} - \mathcal{I})\mathbf{v}^* = \mathbf{v}^*, \quad (8)$$

where  $\mathbf{v}^* \stackrel{\text{def}}{=} [\mathbf{v}_1^*; \dots; \mathbf{v}_N^*] \in \mathbb{R}^{nN}$ , and  $\mathcal{F}, \mathcal{G} : \mathbb{R}^{nN} \rightarrow \mathbb{R}^{nN}$  are mappings defined as

$$\mathcal{F}(\mathbf{z}) = \begin{bmatrix} F_1(\mathbf{z}_1) \\ \vdots \\ F_N(\mathbf{z}_N) \end{bmatrix}, \quad \text{and} \quad \mathcal{G}(\mathbf{z}) = \begin{bmatrix} \langle \mathbf{z} \rangle \\ \vdots \\ \langle \mathbf{z} \rangle \end{bmatrix}, \quad (9)$$

where  $\langle \mathbf{z} \rangle \stackrel{\text{def}}{=} \frac{1}{N} \sum_{i=1}^N \mathbf{z}_i$  is the average of  $\mathbf{z}$ .

*Proof.* See Appendix.  $\square$

Theorem (1) provides a full characterization of the MACE solution. The operator  $\mathcal{G}$  in Theorem 1 is a consensus agent that takes a set of inputs  $\mathbf{z}_1, \dots, \mathbf{z}_N$  and maps them to their average  $\langle \mathbf{z} \rangle$ . In fact, we can show that  $\mathcal{G}$  is a projection and that  $(2\mathcal{G} - \mathcal{I})$  is its self-inverse. (See Appendix.) What this means is that (8) is equivalent to  $(2\mathcal{F} - \mathcal{I})\mathbf{v}^* = (2\mathcal{G} - \mathcal{I})\mathbf{v}^*$ . That is, we want the individual agents  $F_1, \dots, F_N$  to match with the consensus agent  $\mathcal{G}$  such that the equilibrium holds:  $(2\mathcal{F} - \mathcal{I})\mathbf{v}^* = (2\mathcal{G} - \mathcal{I})\mathbf{v}^*$ .

Theorem 1 provides us an algorithm to find the consensus equilibrium state  $\mathbf{x}^*$ . According to (8),  $\mathbf{v}^*$  is a fixed point of the set of equilibrium equations. Finding the fixed point can be done by iteratively updating  $\mathbf{v}^{(k)}$  through the procedure

$$\mathbf{v}^{(k+1)} = (2\mathcal{G} - \mathcal{I})(2\mathcal{F} - \mathcal{I})\mathbf{v}^{(k)}. \quad (10)$$

When  $\mathbf{v}^{(k)}$  converges to  $\mathbf{v}^*$ , then by (7) we can define the solution

$$\mathbf{x}^* = \frac{1}{N} \sum_{i=1}^N \mathbf{v}_i^*. \quad (11)$$

At the equilibrium, the sum of the residues  $\mathbf{u}_1^*, \dots, \mathbf{u}_N^*$  vanishes so that  $\sum_{i=1}^N \mathbf{u}_i^* = 0$ . This means that the ‘‘net tension’’ of the system is zero.

The overall algorithm of the MACE is illustrated in the block diagram shown in Figure 4. In the particular problem of foreground extraction, we also have external inputs marked by the yellow arrows on the left hand side of the figure. These external inputs are signals that do not change over the MACE iteration. For example, for the dual-layer alpha matting agent (See Section 3.1) we need both the color image and the plate image as external inputs.

It is possible to modify (10) to speed up the convergence, e.g., by introducing a damping constant  $\gamma$  such that

$$\mathbf{v}^{(k+1)} = (1 - \gamma)\mathbf{v}^{(k)} + \gamma(2\mathcal{G} - \mathcal{I})(2\mathcal{F} - \mathcal{I})\mathbf{v}^{(k)}, \quad (12)$$



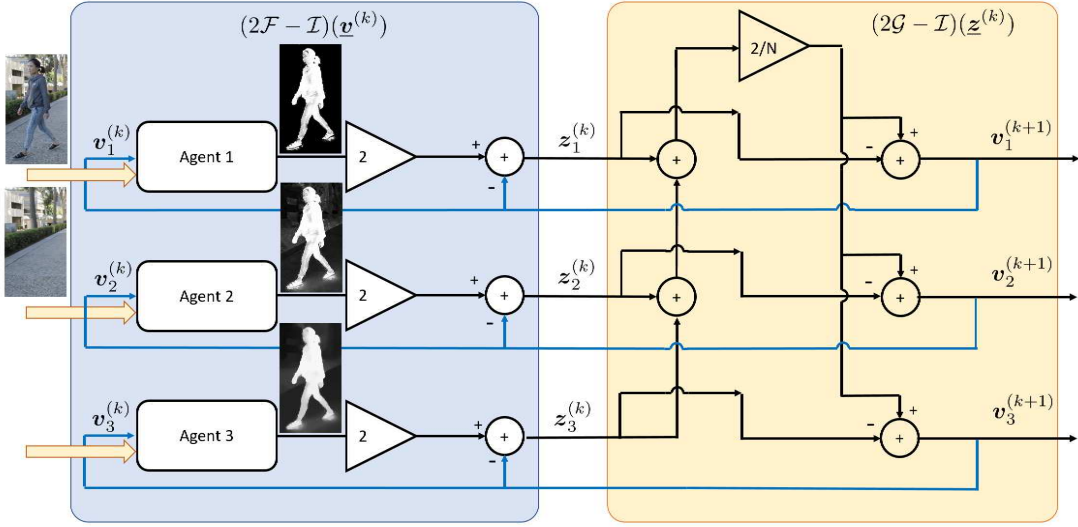


Fig. 4. Overview of the proposed method. Starting with a pair of color and plate images, we iteratively apply  $(2\mathcal{G} - \mathcal{I})(2\mathcal{F} - \mathcal{I})$  until convergence.

for some  $0 < \gamma < 1$ . If  $N = 2$  and  $\gamma = 1/2$ , one can show that (12) becomes the classic Douglas-Rachford splitting.

The convergence of MACE is guaranteed under a few technical conditions on  $\mathcal{F}$ , e.g., being firmly non-expansive or at least locally firmly non-expansive. Non-expansiveness can be satisfied if the function  $f_i$  used to generate  $F_i$  is closed, proper and convex on  $\mathbb{R}^n$ . We will defer the discussion to Section 3.6 after we introduce all the agents in the next section.

## 2.4 Apply MACE to Foreground Extraction

The key question we need to address here is that for the foreground extraction problem, what kind of agents should we use? There are multiple considerations.

First, we need to properly define the signal space for each individual agent because the consensus agent  $\mathcal{G}$  needs to take the average of the agents  $F_1, \dots, F_N$ . If the output spaces of  $F_1, \dots, F_N$  are different, we will not be able to define the averaging operator  $\mathcal{G}$ .

Second, how many agents should we include? In principle, MACE can support any finite number of agents. However, in practice the number of agents should be limited to only a few “good” agents. Here, by “good” we meant that the agent has good performance and complements other agents. For example, MACE is less effective if one is uniformly superior than the rest, because then we can simply pick the best one.

Third, we need to define a feedback mechanism so that the consensus generated by  $\mathcal{G}$  can be used to update  $\mathcal{F}$ . This means that one cannot simply use an off-the-shelf algorithm unless a feedback is naturally built in. For example, it would be very difficult to directly use an off-the-shelf alpha matting algorithm as an agent.

## 3 DESIGNING MACE AGENTS

In this section we describe the three agents used in this paper. We emphasize that the choice of these three agents

are flexible. What we are presenting here is a particular configuration which shows a good balance between runtime, model interpretability and foreground mask quality.

### 3.1 Agent 1: Dual-Layer Closed-Form Matting

The first agent we use in MACE is a modified version of the classic closed-form matting. More precisely, we define the agent as

$$F_1(z) = \underset{\alpha}{\operatorname{argmin}} \quad \alpha^T \tilde{L} \alpha + \lambda_1 (\alpha - z)^T \tilde{D} (\alpha - z), \quad (13)$$

where  $\tilde{L}$  and  $\tilde{D}$  are matrices, and will be explained below. The constant  $\lambda_1$  is a parameter.

**Review of Closed-Form Matting.** To understand the meaning of (13), we recall that the classical closed-form matting assumes a linear model of the alpha matte:

$$\alpha_i \approx \sum_{c \in \{r, g, b\}} a^c I_i^c + b, \quad (14)$$

where  $(a^r, a^g, a^b, b)$  are the linear combination coefficients of the color line model, and  $\alpha_i$  is the alpha matte value of the  $i$ th pixel. The alpha matte can be found by minimizing the energy function

$$J(\alpha, a, b) = \sum_{j \in I} \left( \sum_{i \in w_j} \left( \alpha_i - \sum_c a_j^c I_i^c - b_j \right)^2 + \epsilon \sum_c (a_j^c)^2 \right), \quad (15)$$

where  $w_j$  is a  $3 \times 3$  window of pixel  $j$ . With some algebra, one can show that the marginalized energy function  $J(\alpha) \stackrel{\text{def}}{=} \min_{a, b} J(\alpha, a, b)$  is equivalent to

$$J(\alpha) \stackrel{\text{def}}{=} \min_{a, b} J(\alpha, a, b) = \alpha^T L \alpha, \quad (16)$$

where  $L \in \mathbb{R}^{n \times n}$  is the so-called matting Laplacian matrix. When trimap is given, we can regularize  $J(\alpha)$  by minimizing the overall energy function:

$$\hat{\alpha} = \underset{\alpha}{\operatorname{argmin}} \quad \alpha^T L \alpha + \lambda (\alpha - z)^T D (\alpha - z), \quad (17)$$

where  $D$  is a binary diagonal matrix with entries being one for pixels that are labeled in the trimap, and zero otherwise. The vector  $z \in \mathbb{R}^n$  contains specified alpha values given by the trimap. Thus, for large  $\lambda$ , the minimization in (17) will force the solution to satisfy the constraints given by the trimap. (See [20] for details.)

There are multiple reason why (17) is inadequate for our problem. First, (17) requires a good trimap. If there are false alarms or misses in the trimap, results returned by (17) will be heavily biased towards these errors because of the large  $\lambda$ . Second, in our problem we need to incorporate the plate image into the algorithm, which implies that the matrix  $L$  needs to be defined differently.

**Dual-Layer Matting Laplacian  $\tilde{L}$ .** In the presence of the plate image, we have two pieces of complementary information:  $I \in \mathbb{R}^{n \times 3}$  the color image containing the foreground object, and  $P \in \mathbb{R}^{n \times 3}$  the plate image. Correspondingly, we have alpha matte  $\alpha^I$  for  $I$ , and the alpha matte  $\alpha^P$  for  $P$ . (Ideally,  $\alpha^P = 0$  because it does not contain any foreground.) When  $P$  is given, we can redefine (14) as

$$\begin{bmatrix} \alpha_i^I \\ \alpha_i^P \end{bmatrix} \approx \sum_{c \in \{r, g, b\}} a^c \begin{bmatrix} I_i^c \\ P_i^c \end{bmatrix} + b. \quad (18)$$

In other words, we ask the coefficients  $(a^r, a^g, a^b, b)$  to fit simultaneously the actual image  $I$  and the plate image  $P$ . When (18) is assumed, the energy function  $J(\alpha, a, b)$  becomes

$$\begin{aligned} \tilde{J}(\alpha^I, \alpha^P, a, b) = & \sum_j \left\{ \sum_{i \in w_j} \left( \alpha_i^I - \sum_c a_j^c I_i^c - b_j \right)^2 \right. \\ & \left. + \eta \sum_{i \in w_j} \left( \alpha_i^P - \sum_c a_j^c P_i^c - b_j \right)^2 + \epsilon \sum_c (a_j^c)^2 \right\}, \quad (19) \end{aligned}$$

where we added a constant  $\eta$  to regulate the relative emphasis between  $I$  and  $P$ .

The difference between (19) and (15) is the additional plate term. However, since (19) remains a quadratic equation, we can expect an expression similar to (16). The following proposition provides some details.

**Theorem 2.** *The marginal energy function*

$$\tilde{J}(\alpha) \stackrel{\text{def}}{=} \min_{a, b} \tilde{J}(\alpha, a, b) \quad (20)$$

can be equivalently expressed as  $\tilde{J}(\alpha) = \alpha^T \tilde{L} \alpha$ , where  $\tilde{L} \in \mathbb{R}^{n \times n}$  is the modified matting Laplacian, with the  $(i, j)$ th element

$$\begin{aligned} \tilde{L}_{i,j} = & \sum_{k|(i,j) \in w_k} \left\{ \delta_{ij} - \frac{1}{2|w_k|} \left( 1 + (I_i - \mu_k)^T \right. \right. \\ & \left. \left. (\Sigma_k - n(1+\eta)\mu_k\mu_k^T)^{-1} (I_j - \mu_k) \right) \right\}. \quad (21) \end{aligned}$$

Here,  $\delta_{ij}$  is the Kronecker delta,  $I_i \in \mathbb{R}^3$  is the color vector at the  $i$ th pixel. The vector  $\mu_k \in \mathbb{R}^3$  is defined as

$$\mu_k = \frac{1}{2|w_k|} \sum_{j \in w_k} (I_j + P_j), \quad (22)$$

and the matrix  $\Sigma_k \in \mathbb{R}^{3 \times 3}$  is

$$\begin{aligned} \Sigma_k = & \frac{1}{2} \left\{ \frac{1}{|w_k|} \sum_{j \in w_k} (I_j - \mu_k)(I_j - \mu_k)^T \right. \\ & \left. + \frac{1}{|w_k|} \sum_{j \in w_k} (P_j - \mu_k)(P_j - \mu_k)^T \right\}. \quad (23) \end{aligned}$$

*Proof.* See Appendix.  $\square$

Because of the plate term in (19), the modified matting Laplacian  $\tilde{L}$  is positive definite. See Appendix for proof. The original  $L$  in (16) is only positive semi-definite.

**Dual-Layer Regularization  $\tilde{D}$ .** The diagonal regularization matrix  $\tilde{D}$  in (13) is reminiscent to the binary matrix  $D$  in (17), but  $\tilde{D}$  is defined through a sigmoid function applied to the input  $z$ . To be more precise, we define  $\tilde{D} \stackrel{\text{def}}{=} \text{diag}(\tilde{d}_i)$ , where

$$\tilde{d}_i = \text{diag} \left\{ \frac{1}{1 + \exp\{-\kappa(z_i - \theta)\}} \right\} \in \mathbb{R}^{n \times n}, \quad (24)$$

and  $z_i$  is the  $i$ -th element of the vector  $z \in \mathbb{R}^n$ , which is the argument of  $F_1$ . The scalar constant  $\kappa > 0$  is a user defined parameter specifying the stiffness of the sigmoid function, and  $0 < \theta < 1$  is another user defined parameter specifying the center of the transient. Typical values of  $(\kappa, \theta)$  for our MACE framework are  $\kappa = 30$  and  $\theta = 0.8$ .

A closer inspection of  $D$  and  $\tilde{D}$  reveals that  $D$  is performing a hard-threshold whereas  $\tilde{D}$  is performing a soft-threshold. In fact, the matrix  $D \stackrel{\text{def}}{=} \text{diag}(d_i)$  has diagonal entries

$$d_i = \begin{cases} 0, & \theta_1 < z_i < \theta_2, \\ 1, & \text{otherwise.} \end{cases} \quad (25)$$

for two cutoff values  $\theta_1$  and  $\theta_2$ . This hard-threshold is equivalent to the soft-threshold in (24) when  $\kappa \rightarrow \infty$ .

There are a few reasons why (24) is preferred over (25), especially when we have the plate image. First, the soft-threshold in (24) tolerates more error present in  $z$ , because the values of  $\tilde{D}$  represent the probability of having foreground pixels. Second, the one-sided threshold in (24) ensures that the background portion of the image is handled by the plate image rather than the input  $z$ . This is usually beneficial when the plate is reasonably accurate.

To satisfy the theoretical convergence criteria for the MACE algorithm (which we will discuss in Section 3.5), we iteratively reduce  $\kappa$  by

$$\kappa^{(t+1)} = \beta \kappa^{(t)},$$

for some constant  $\beta < 1$ , and set  $\kappa^{(t)} = 0$  if  $t > t_{\max}$  for some maximum number of iterations. When this happens, we have

$$\tilde{D}^{(t)} = (1/2)I, \quad \text{if } t > t_{\max}. \quad (26)$$

In this paper, we update  $\tilde{D}$  using  $t_{\max} = 30$  iterations, and keep  $\tilde{D}$  unchanged for the remaining of the iterations.

### 3.2 Agent 2: Background Estimator

Our second agent is a background estimator, defined as

$$F_2(\mathbf{z}) = \underset{\alpha}{\operatorname{argmin}} \quad \|\alpha - \mathbf{r}_0\|^2 + \lambda_2 \|\alpha - \mathbf{z}\|^2 + \gamma \alpha^T (1 - \alpha). \quad (27)$$

The reason of introducing  $F_2$  is that in  $F_1$ , the matrix  $\mathbf{D}$  is determined by the current estimate  $\mathbf{z}$ . While  $\mathbf{D}$  handles part of the error in  $\mathbf{z}$ , large missing pixels and false alarms can still cause problems especially in the interior regions. The goal of  $F_2$  is to complement  $F_1$  for these interior regions.

**Initial Background Estimate  $\mathbf{r}_0$ .** Let us take a look at (27). The first two terms are quadratic. The interpretation is that given some fixed initial estimate  $\mathbf{r}_0$  and the current input  $\mathbf{z}$ ,  $F_2(\mathbf{z})$  returns a linearly combined estimate between  $\mathbf{r}_0$  and  $\mathbf{z}$ . The initial estimate  $\mathbf{r}_0$  consists of two parts:

$$\mathbf{r}_0 = \mathbf{r}_c \odot \mathbf{r}_e, \quad (28)$$

where  $\odot$  means elementwise multiplication. The first term  $\mathbf{r}_c$  is the *color* term, measuring the similarity between foreground and background colors. The second term  $\mathbf{r}_e$  is the *edge* term, measuring the likelihood of foreground edges relative background edges. In the followings we will discuss these two terms one by one.

**Defining the Color Term  $\mathbf{r}_c$ .** We define  $\mathbf{r}_c$  by measuring the distance  $\|\mathbf{I}_j - \mathbf{P}_j\|^2 = \sum_{c \in \{r, g, b\}} (I_j^c - P_j^c)^2$  between a color pixel  $\mathbf{I}_j \in \mathbb{R}^3$  and a plate pixel  $\mathbf{P}_j \in \mathbb{R}^3$ . Ideally, we would like  $\mathbf{r}_c$  to be small when  $\|\mathbf{I}_j - \mathbf{P}_j\|^2$  is large.

In order to improve the robustness of  $\|\mathbf{I}_j - \mathbf{P}_j\|^2$  against noise and illumination fluctuation, we modify  $\|\mathbf{I}_j - \mathbf{P}_j\|^2$  by using the bilateral weighted average over a small neighborhood:

$$\Delta_i = \sum_{j \in \Omega_i} w_{ij} \|\mathbf{I}_j - \mathbf{P}_j\|^2, \quad (29)$$

where  $\Omega_i$  specifies a small window around the pixel  $i$ . The bilateral weight  $w_{ij}$  is defined as

$$w_{ij} = \frac{\tilde{w}_{ij}}{\sum_j \tilde{w}_{ij}}, \quad (30)$$

where

$$\tilde{w}_{ij} = \exp \left\{ -\frac{\|\mathbf{x}_i - \mathbf{x}_j\|^2}{2h_s^2} \right\} \exp \left\{ -\frac{\|\mathbf{I}_i - \mathbf{I}_j\|^2}{2h_r^2} \right\}. \quad (31)$$

Here,  $\mathbf{x}_i$  denotes the spatial coordinate of pixel  $i$ ,  $\mathbf{I}_i \in \mathbb{R}^3$  denotes the  $i$ th color pixel of the color image  $\mathbf{I}$ , and  $(h_s, h_r)$  are the parameters controlling the bilateral weight strength.

We now need a mapping which maps the distance  $\Delta \stackrel{\text{def}}{=} [\Delta_1, \dots, \Delta_n]^T$  to a vector of numbers  $\mathbf{r}_c$  in  $[0, 1]^n$  so that the term  $\|\alpha - \mathbf{r}_0\|^2$  makes sense. To this end, we choose a simple Gaussian function:

$$\mathbf{r}_c = 1 - \exp \left\{ -\frac{\Delta^2}{2\sigma_\delta^2} \right\}, \quad (32)$$

where  $\sigma_\delta$  is a user tunable parameter. We tested other possible mappings such as the sigmoid function and the cumulative distribution function of a Gaussian. However, we do not see significant difference compared to (32).

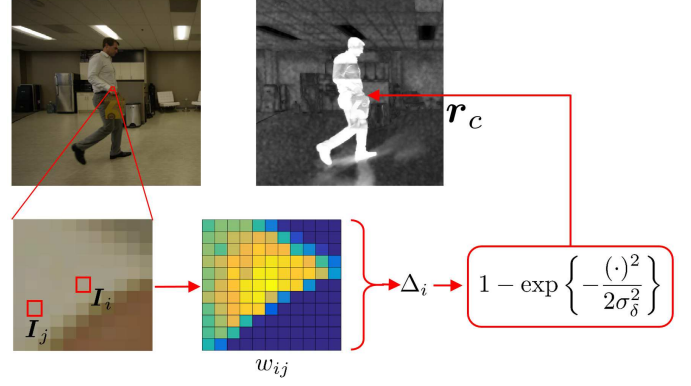


Fig. 5. Illustration of how to construct the estimate  $\mathbf{r}_c$ . We compute the distance between the foreground and the background. The distance has a bilateral weight to improve robustness. The actual  $\mathbf{r}_0$  represents the probability of having a foreground pixel.

**Defining the Edge Term  $\mathbf{r}_e$ .** The color term  $\mathbf{r}_c$  is able to capture most of the difference between the image and the plate. However, it also generates false alarms if there is illumination change. For example, shadow due to the foreground object is often falsely labeled as foreground. In Figure 5, we show an example where shadow causes false alarm near the foot.

In order to reduce the false alarm due to minor illumination change, we first create a “super-pixel” mask by grouping similar colors. Our super-pixels are generated by applying a standard flood-fill algorithm [44] to the image  $\mathbf{I}$ . This gives us a partition of the image  $\mathbf{I}$  as

$$\mathbf{I} \rightarrow \{\mathbf{I}^{S_1}, \mathbf{I}^{S_2}, \dots, \mathbf{I}^{S_m}\}, \quad (33)$$

where  $S_1, \dots, S_m$  are the  $m$  super-pixel index sets. The plate image is partition using the same super-pixel indices, i.e.,  $\mathbf{P} \rightarrow \{\mathbf{P}^{S_1}, \mathbf{P}^{S_2}, \dots, \mathbf{P}^{S_m}\}$ .

While we are generating the super-pixels, we also compute the gradients of  $\mathbf{I}$  and  $\mathbf{P}$  for every pixel  $i = 1, \dots, n$ . Specifically, we define  $\nabla \mathbf{I}_i = [\nabla_x \mathbf{I}_i, \nabla_y \mathbf{I}_i]^T$  and  $\nabla \mathbf{P}_i = [\nabla_x \mathbf{P}_i, \nabla_y \mathbf{P}_i]^T$ , where  $\nabla_x \mathbf{I}_i \in \mathbb{R}^3$  (and  $\nabla_y \mathbf{I}_i \in \mathbb{R}^3$ ) are the two-tap horizontal (and vertical) finite difference at the  $i$ -th pixel. To measure how far  $\mathbf{I}_i$  is from  $\mathbf{P}_i$ , we compute

$$\theta_i = \|\nabla \mathbf{I}_i - \nabla \mathbf{P}_i\|_2. \quad (34)$$

Thus,  $\theta_i$  is small for background regions because  $\mathbf{I}_i \approx \mathbf{P}_i$ , but is large when there is a foreground pixel in  $\mathbf{I}_i$ . If we set a threshold operation after  $\theta_i$ , i.e., set  $\theta_i = 1$  if  $\theta_i > \tau_\theta$  for some threshold  $\tau_\theta$ , then shadows can be removed as their gradients are weak.

Now that we have computed  $\theta_i$ , we still need to map it back to a quantity similar to the alpha matte. To this end, we compute a normalization term

$$A_i = \max(\|\nabla \mathbf{I}_i\|_2, \|\nabla \mathbf{P}_i\|_2), \quad (35)$$

and normalize  $\mathbb{1}\{\theta_i > \tau_\theta\}$  by

$$(r_e)_i \stackrel{\text{def}}{=} \frac{\sum_{j \in S_i} \mathbb{1}\{A_i > \tau_A\} \mathbb{1}\{\theta_i > \tau_\theta\}}{\sum_{j \in S_i} \mathbb{1}\{A_i > \tau_A\}}, \quad (36)$$

where  $\mathbb{1}$  denotes the indicator function, and  $\tau_A$  and  $\tau_\theta$  are thresholds. In essence, (36) says in the  $i$ -th super-pixel  $S_i$ , we count the number of edges  $\mathbb{1}\{\theta_i > \tau_\theta\}$  that have strong

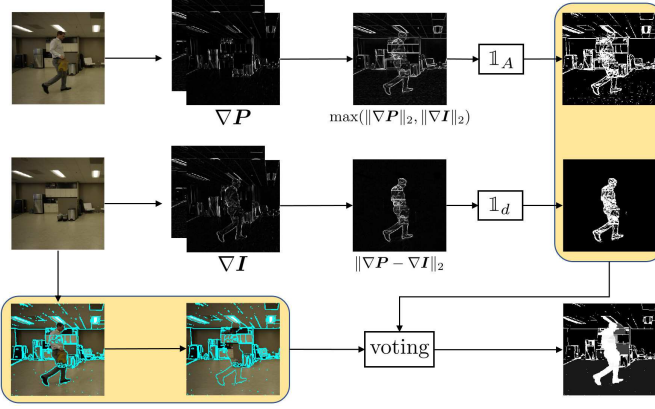


Fig. 6. Illustration of how to construct the estimate  $r_e$ .

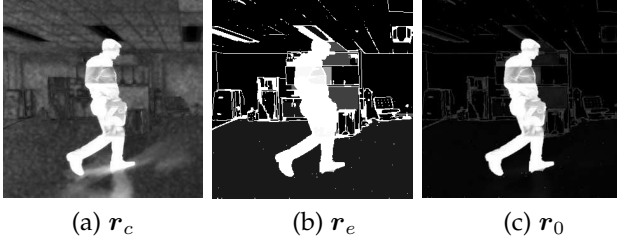


Fig. 7. Comparison between  $r_c$ ,  $r_e$ , and  $r_0$ .

difference between  $I_i$  and  $P_i$ . However, we do not want to count every pixel but only pixels that already contains strong edges, either in  $I$  or  $P$ . Thus, we take the weighted average using  $\mathbb{1}\{A_i > \tau_A\}$  as the weight. This defines  $r_e$ , as the weighted average  $(r_e)_i$  is shared among all pixels in the super-pixel  $S_i$ . Figure 6 shows a pictorial illustration.

Why is  $r_e$  helpful? If we take a close inspection at  $r_c$  and  $r_e$  in Figure 7, it is not difficult to see that foreground pixels of  $r_c$  and  $r_e$  coincide but background pixels roughly cancels each other. The reason is that while  $r_c$  tends to create weak holes in the foreground,  $r_e$  fills the gap by ensuring the foreground is marked.

**Regularization  $\alpha^T(1 - \alpha)$ .** The last term  $\alpha^T(1 - \alpha)$  in (27) is a regularization to force the solution to either 0 or 1. The effect of this term can be seen from the fact that  $\alpha^T(1 - \alpha)$  is a symmetric concave quadratic function with a value zero for  $\alpha = 1$  or  $\alpha = 0$ . Therefore, it introduces penalty for solutions that are away from 0 or 1. For  $\gamma \leq 1$ , one can show that the Hessian matrix of the function  $f_2(\alpha) = \|\alpha - r_0\|^2 + \gamma\alpha^T(1 - \alpha)$  is positive semidefinite. Thus,  $f_2$  is strongly convex with parameter  $\gamma$ .

Finally, we notice that (27) is quadratic and so closed-form solution exists:

$$v = \frac{r_0 + \lambda_2 z - \gamma}{1 + \lambda_2 - \gamma}. \quad (37)$$

### 3.3 Agent 3: Total Variation Denoising

The third agent we use in MACE is a total variation denoising operator, defined as [45]

$$F_3(z) = \operatorname{argmin}_{\alpha} \|\alpha\|_{TV} + \lambda_3 \|\alpha - z\|^2, \quad (38)$$

where  $\lambda_3$  is a parameter. In general,  $\|\cdot\|_{TV}$  is defined in space-time:

$$\|v\|_{TV} \stackrel{\text{def}}{=} \sum_{i,j,t} \sqrt{\beta_x (\nabla_x v)^2 + \beta_y (\nabla_y v)^2 + \beta_t (\nabla_t v)^2}, \quad (39)$$

where  $(\beta_x, \beta_y, \beta_t)$  controls the relative strength of the gradient in each direction. In this paper, for spatial total variation we set  $(\beta_x, \beta_y, \beta_t) = (1, 1, 0)$ , and for spatial-temporal total variation we set  $(\beta_x, \beta_y, \beta_t) = (1, 1, 0.25)$ .

The choice of the total variation denoising operation is more or less the result of balancing complexity and performance. Users can use stronger denoisers such as BM3D (or BM4D for videos) or non-local means. However, these patch based image denoising algorithms rely on the patch matching procedure, and so they tend to under-smooth repeated patterns of false alarm / misses. Neural network denoisers are better candidates but they need to be trained with the specifically distorted alpha mattes. From our experience, we do not see any particular advantage of using CNN-based denoisers. Figure 8 shows some comparison.

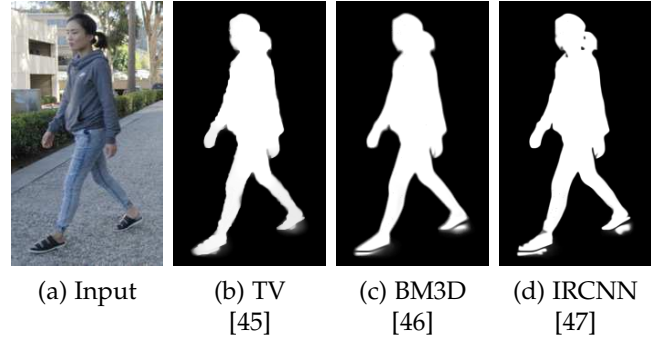


Fig. 8. Comparison of difference denoisers used in MACE. Shown are the results when MACE converges. The shadow near the foot is a typical place of false alarm, and many denoisers cannot handle.

### 3.4 MACE Algorithm

Integrating the above agents, we show in Algorithm 1 the overall MACE algorithm. In this algorithm, the matting Laplacian  $\tilde{L}$  and the initial probability estimate  $r_0$  are pre-calculated, whereas the variables  $z_1^t, z_2^t, z_3^t$  are initialized to  $r_0$ . During each iteration, the agents  $F_1, F_2$  and  $F_3$  first independently process the  $z_i^t$ 's and generate new estimates  $\alpha_i^t$  (for  $i = 1, 2, 3$ ). The main MACE step is then to compute  $(2\mathcal{F} - \mathcal{I})$ , followed by  $(2\mathcal{G} - \mathcal{I})$ . Note that because of the way we perform  $F_i$ 's, the agents are executed in *parallel*. This makes one difference with the traditional ADMM algorithm which performs the steps sequentially.

### 3.5 What Does MACE Try to Solve?

The solution returned by MACE can be roughly understood by writing out an overall optimization. If we assume  $t > t_{\max}$  so that  $\tilde{D} = I$ , then all agents are proximal operators. The corresponding optimization is therefore

$$\operatorname{argmin}_{\alpha} \alpha^T \tilde{L} \alpha + \kappa_1 \|\alpha - r_0\|^2 + \kappa_2 \alpha^T(1 - \alpha) + \kappa_3 \|\alpha\|_{TV}, \quad (40)$$

for appropriate choices of parameters  $\kappa_1, \kappa_2, \kappa_3$ . In this optimization, the solution is characterized by the matting



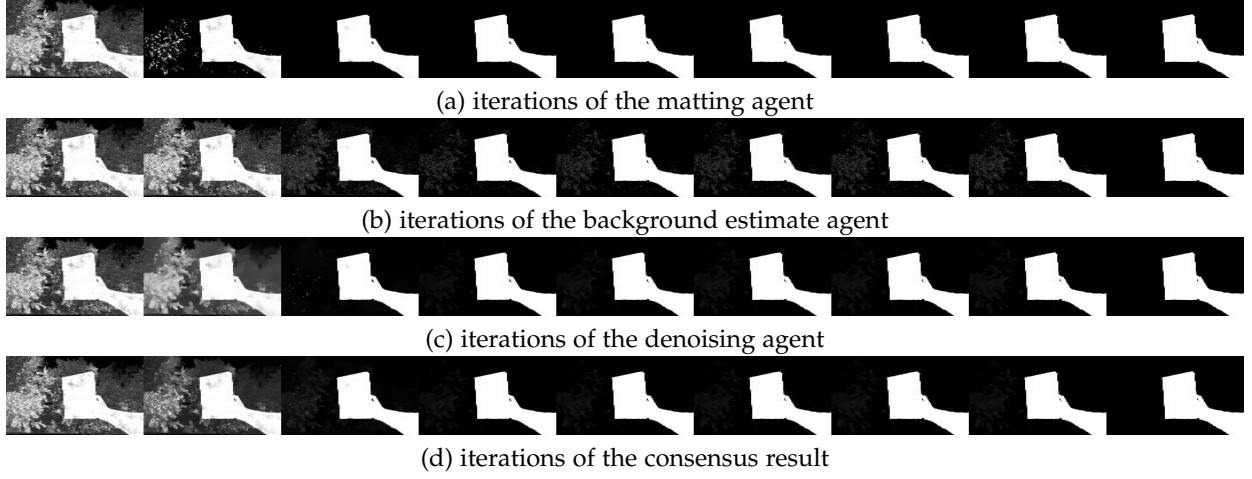


Fig. 9. Evolution of the iterates. The first column is  $r_0$ , followed by results of iteration 1, 5, 10, 15, 20, 25, 30, 35.

---

**Algorithm 1** MACE Algorithm
 

---

```

1: Input  $\tilde{L}, r_0$ .
2: Initialize  $z_1^1 = z_2^1 = z_3^1 = r_0$ .
3: for  $t = 1, \dots, T$  do
4:   % Perform agent updates in parallel
5:   Update  $\tilde{D}_t$  using  $z_1^t$ .
6:    $\alpha_1^t = \underset{\alpha}{\operatorname{argmin}} \quad \alpha^T \tilde{L} \alpha + \lambda_1 (\alpha - z_1^t)^T \tilde{D}_t (\alpha - z_1^t)$ 
7:    $\alpha_2^t = \underset{\alpha}{\operatorname{argmin}} \quad \|\alpha - r_0\|^2 + \lambda_2 \|\alpha - z_2^t\|^2 + \gamma \alpha^T (1 - \alpha)$ 
8:    $\alpha_3^t = \underset{\alpha}{\operatorname{argmin}} \quad \|\alpha\|_{TV} + \lambda_3 \|\alpha - z_3^t\|^2$ 
9:
10:  % Perform the operation  $(2\mathcal{F} - \mathcal{I})$ 
11:   $v_1^t = 2\alpha_1^t - z_1^t$ 
12:   $v_2^t = 2\alpha_2^t - z_2^t$ 
13:   $v_3^t = 2\alpha_3^t - z_3^t$ 
14:
15:  % Perform the operation  $(2\mathcal{G} - \mathcal{I})$ 
16:   $\langle v^t \rangle = (v_1^t + v_2^t + v_3^t) / 3$ 
17:   $z_1^{t+1} = 2\langle v^t \rangle - v_1^t$ 
18:   $z_2^{t+1} = 2\langle v^t \rangle - v_2^t$ 
19:   $z_3^{t+1} = 2\langle v^t \rangle - v_3^t$ 
20: end for
21: Output  $\langle v^t \rangle$ .
```

---

Laplacian  $\tilde{L}$ , with trade-offs between similarity with  $r_0$ , disparity of  $\alpha$  from 0 and 1, and smoothness according to total variation. The fixed point algorithm of the MACE then corresponds to a classical ADMM algorithm where there are multiple variable splittings.

What is *not* captured by (40) is the evolution of the matrix  $\tilde{D}$ , because technically speaking  $\tilde{D}$  should be  $\tilde{D}(z)$ , i.e., a function of the input  $z$  to the proximal map  $F_1$ . The dynamics of  $\tilde{D}$  will cause the solution to land on a different minimizer of (40). (Note that (40) is convex but not strictly convex, and so the global minimum is not unique.) Therefore, while (40) provides a rough picture of the solution, the actual solution returned by the MACE algorithm can only be described as a fixed point among the agents. The evolution of the agents is illustrated in Figure 9.

### 3.6 Convergence and Runtime

We finally comment on the convergence of MACE. The convergence of MACE is guaranteed when  $\mathcal{T} \stackrel{\text{def}}{=} (2\mathcal{G} - \mathcal{I})(2\mathcal{F} - \mathcal{I})$  is non-expansive [39]. This, in turn, requires firmly non-expansiveness of  $\mathcal{F}$  and  $\mathcal{G}$ . We summarize these in the following lemma.

**Lemma 1.** *Let  $\mathcal{F}$  and  $\mathcal{G}$  be defined as (9), and let  $\mathcal{T} \stackrel{\text{def}}{=} (2\mathcal{G} - \mathcal{I})(2\mathcal{F} - \mathcal{I})$ . Then the following results hold:*

- (i)  $\mathcal{F}$  is firmly non-expansive if all  $F_i$ 's are firmly non-expansive.
- (ii)  $\mathcal{G}$  is firmly non-expansive.
- (iii)  $\mathcal{T}$  is non-expansive if  $\mathcal{F}$  and  $\mathcal{G}$  are firmly non-expansive.

*Proof.* See Appendix. □

The key challenge now is to prove that all the three  $F_i$ 's we use in this paper are firmly non-expansive. To this end, we need the following lemma.

**Lemma 2.** *Assume  $\tilde{D} = (1/2)\mathbf{I}$  after  $t_{\max}$  iterations, i.e., (26) holds. Then, the  $F_i$ 's defined in (13), (27), and (38) are firmly non-expansive.*

*Proof.* See Appendix. □

In terms of runtime, the most time-consuming part is the dual-layer alpha matting agent because we need to solve a large-scale sparse least squares problem. As a result, the runtime of the overall MACE depends on the number of foreground pixels. See Table 1 in Experiment Section for the actual runtime. In generating these results, we used an un-optimized MATLAB code on a Intel i7-4770k. For most of the sequences we tested, the typical runtime is about 1-3 minutes per frame, which can further be improved by porting the algorithms to C++ or GPUs. From our experience working with professional artists, the time for a human to create a ground truth label is at least 15 minutes per frame (for good quality masks). Therefore, the runtime benefit is still substantial.

		resolution	FGD %	time/Fr (sec)	indoor/ outdoor	shadow	lighting issues	Backgrd vibration	camouflage	green screen	ground truth
Purdue Dataset	Book	540x960	19.75%	231	outdoor			✓	✓		✓
	Building	632x1012	4.03%	170.8	outdoor	✓		✓	✓		✓
	Coach	790x1264	4.68%	396.1	outdoor			✓		✓	✓
	Studio	480x270	55.10%	58.3	indoor						✓
	Road	675x1175	1.03%	232.9	outdoor	✓		✓	✓		✓
	Tackle	501x1676	4.80%	210.1	outdoor	✓		✓		✓	✓
	Gravel	790x1536	2.53%	280.1	outdoor	✓		✓	✓		✓
	Office	623x1229	3.47%	185.3	indoor	✓			✓		✓
Public Dataset [18]	Bootstrap	480x640	13.28%	109.1	indoor	✓	✓		✓		✓
	Cespatx	480x640	10.31%	106.4	indoor	✓	✓		✓		✓
	DCam	480x640	12.23%	123.6	indoor	✓	✓		✓		✓
	Gen	480x640	10.23%	100.4	indoor	✓	✓		✓		✓
	Multipeople	480x640	9.04%	99.5	indoor	✓	✓		✓		✓
	Shadow	480x640	11.97%	115.2	indoor	✓	✓				✓

TABLE 1  
Description of the video sequences used in our experiments.

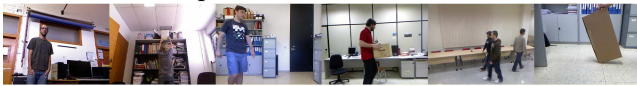
## 4 EXPERIMENTAL RESULTS

### 4.1 Dataset

To evaluate the proposed method, we create a Purdue dataset containing 8 video sequences and select 6 additional video sequences from a public dataset [18], making a total of 14 video sequences. Snapshots of the sequences are shown in Figure 10, and a description of the videos is given in Table 1. All video sequences are captured without camera motion. Plate images are also available, either during the first or the last few frames of the video. To enable objective evaluation, for each video sequence we randomly select 10 frames and manually generate ground truths. Thus totally there are 140 frames with ground truths.



(a) Snapshots of the Purdue Dataset



(b) Snapshots of a public dataset [18]

Fig. 10. Snapshots of the videos we use in the experiment.

The reason of introducing both the Purdue dataset and an existing publicly available dataset is two-fold. First, while there are many background subtraction datasets, e.g., [48]–[51], the resolutions are usually low and the ground truths are coarse. Some datasets contain videos, but the backgrounds could be moving, which is beyond the scope of this paper. Datasets on [alphamatting.com](http://alphamatting.com) and [videomatting.com](http://videomatting.com) are designed for methods with trimaps. The plate images are not available in these datasets. Therefore, we create the Purdue dataset using a high-resolution camera to capture both the videos and the plate image. Second, we like to test the robustness of our algorithm to lower quality videos with lower resolution, more motion blur, and more flickering in the videos. This leads us to consider the dataset by [18] where we select 6 videos for the study.

The characteristics of the dataset is summarized in Table 1. The Purdue dataset has various resolution, and the Public dataset has one resolution  $480 \times 640$ . The foreground percentage for the Purdue dataset videos ranges

from 1.03% to 55.10%, whereas that public dataset has similar foreground percentage around 10%. The runtime of the algorithm (per frame) is determined by the resolution and the foreground percentage. In terms of content, the Purdue dataset focuses on outdoor scenes whereas the public dataset are only indoor. The shadow column indicates the presence of shadow. Lighting issues includes the illumination change due to auto-exposure and auto-white-balance. The backgrn vibration only applies to outdoor scenes where the background objects have minor movements, e.g., moving grass or tree branches. The camouflage column indicates the similarity in color between the foreground and background, which is a common problem for most sequences. The green screen column shows which of the sequences have green screens to mimic the common chroma-keying environment.

### 4.2 Competing methods

We categorize the competing methods into three different categories. The key ideas of the competing methods are summarized in Table 2.

Methods		Automated?	Key idea
PBAS	[19]	full-auto	non-parametric background subtraction
ViBe	[52]	full-auto	pixel model based background subtraction
NLVS	[53]	full-auto	non-local voting video segmentation
BSVS	[29]	semi-auto	bilateral space video segmentation
Matting	[17]	trimap	Trimap generation + alpha matting

TABLE 2  
Description of the competing methods.

- **Full-automatic methods:** We consider two background subtraction algorithms and one video segmentation method in this category : Pixel-based adaptive segmenter (PBAS) [19], ViBe [52], and NLVS [53]. The advantages of PBAS and ViBe are their real-time performance. However, the generated masks are below the requirement of virtual reality we target. NLVS uses optical flow as the main cue and exploits the similarities among super-pixels. Thus it suffers from errors induced in the super-pixel step.

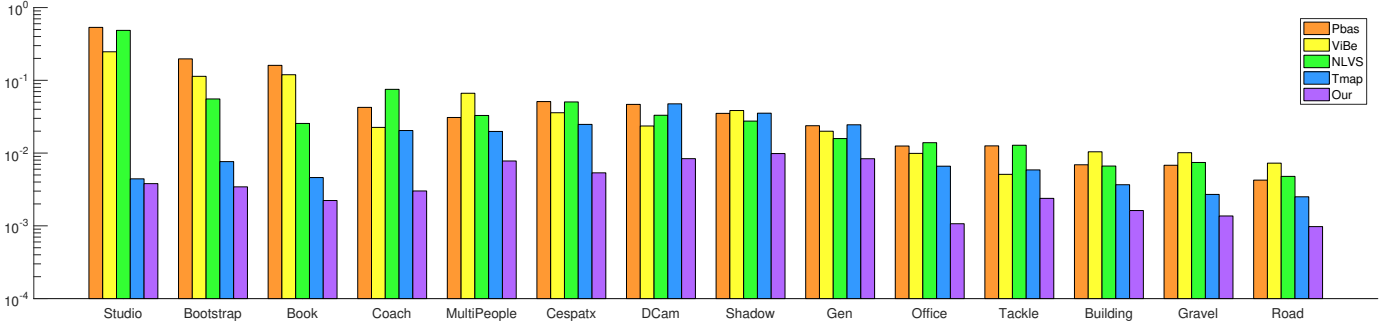


Fig. 11. Comparison with fully automatic methods: PBAS [19], ViBe [52], and NLVS [53], and also Trimap + DCNN [17].

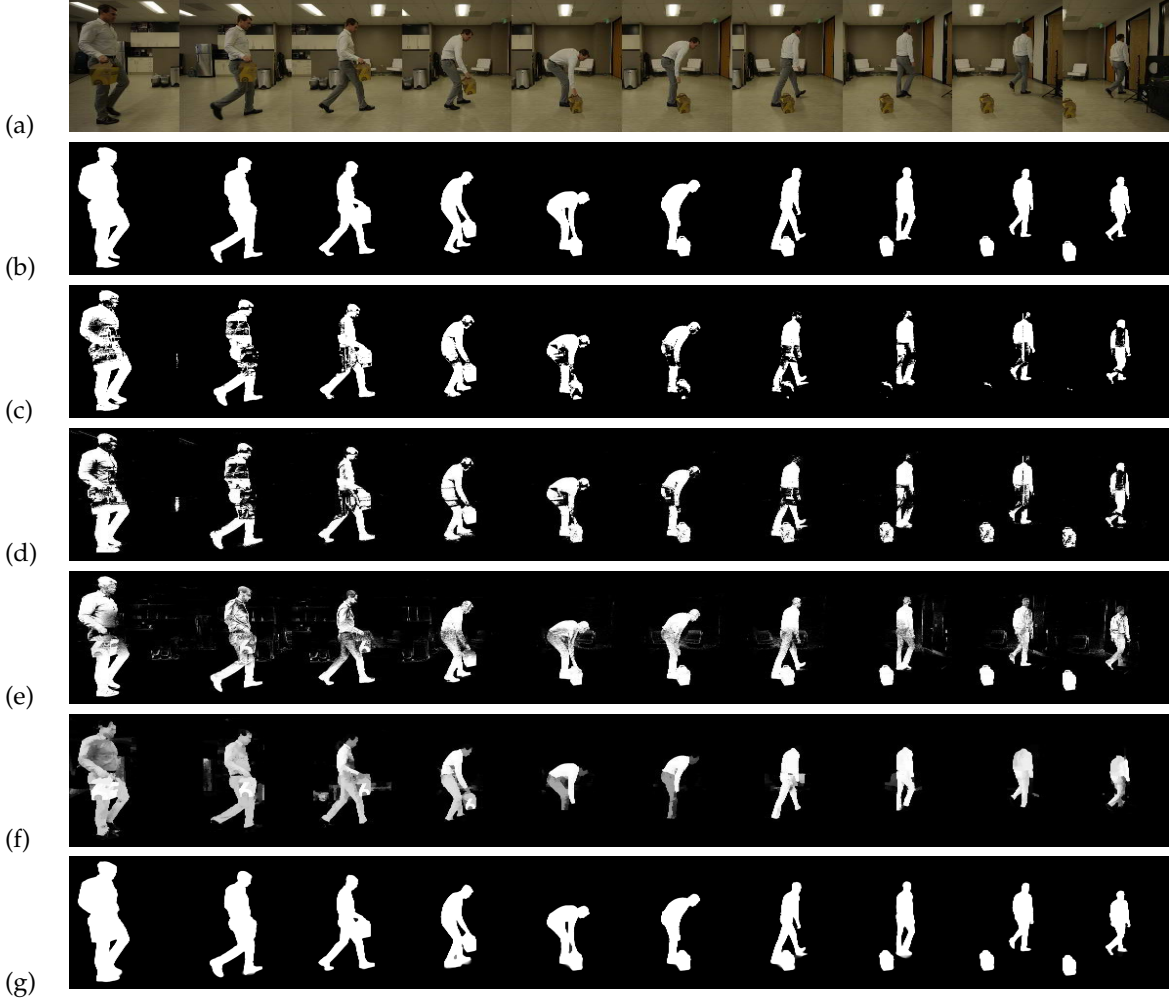


Fig. 12. Office sequence results. (a) Input. (b) Ground truth. (c) PBAS [19]. (d) ViBe [52]. (e) BSVS [29]. (f) NLVS [53]. (g) Ours.

- **Semi-automatic method:** We consider the BSVS [29], a semi-supervised video segmentation algorithm using bilateral space. BSVS is semi-supervised as it requires the user to provide ground truth labels for key frames.
- **Alpha matting using trimap:** We consider one of the state-of-the-art alpha matting algorithm using CNN [17]. The trimaps are generated by applying frame difference between the plate and color images, followed by morphological and thresholding operations.

We emphasize that while these competing methods are the closest to our method, they are considerably different, e.g., BSVS does not require a plate, but it requires key

frames. NLVS does not require a plate, but it cannot handle stationary objects as it relies on optical flow.

### 4.3 Results

We use mean absolute error (MAE) as an evaluation metric. The total MAE contains two parts, false alarm and miss:

$$\text{MAE}_{\text{FA}} = (1/n) \sum_i (\hat{x}_i - x_i, 0)_+,$$

$$\text{MAE}_{\text{miss}} = (1/n) \sum_i (\hat{x}_i - x_i, 0)_-,$$

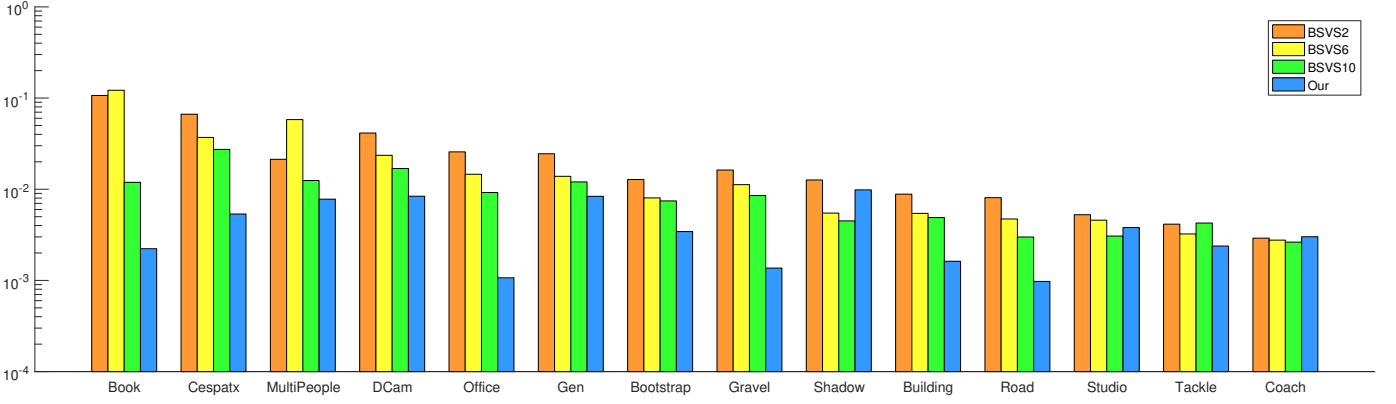


Fig. 13. Comparison with semi-automatic BSVS [29] under different configurations

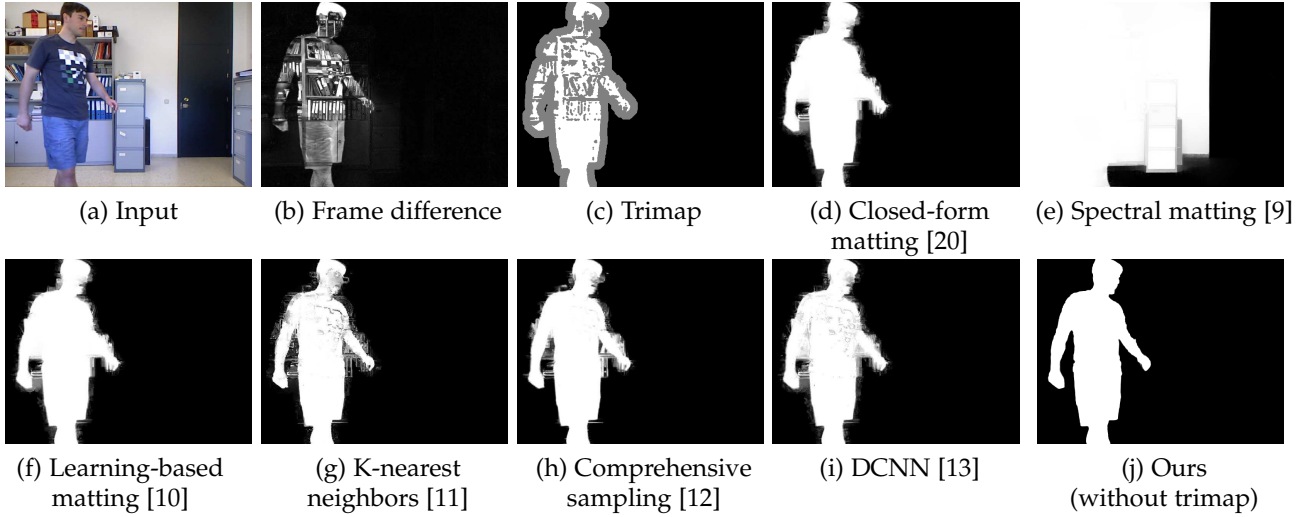


Fig. 14. Comparison with existing alpha-matting algorithms on real images. (a) Input image. (b) Binary mask returned by the standard background subtraction algorithm in OpenCV. (c) Trimap generated by morphographic operation (dilation / erosion) of the binary mask. (d) - (i) Alpha matting algorithms available on [alphamatting.com](http://alphamatting.com). (j) Proposed method.

and  $MAE = MAE_{FA} + MAE_{miss}$ . In this equation,  $\hat{x}_i$  is the  $i$ -pixel of the estimated alpha matte, and  $x_i$  is that of the ground truth. The  $(\cdot)_+$  operator extracts the positive part, and  $(\cdot)_-$  operator extracts the negative part.

• **Comparison with full-automatic methods:** The results are shown in Figure 11, where we plot the overall MAE for different methods. (The detailed break down of miss and false alarms can be found in the Supplementary material.) In this chart, it is clear that the proposed method performs the best. Among the video sequences, the competing methods perform most badly for *studio*, *bootstrap* and *book*, as the foreground object is stationary so that the algorithms treat it as background.

To visually compare the performance, we show snapshots of the *office* sequence in Figure 12. In this figure, we observe that PBAS and ViBe have substantial miss errors due to the similarity between the foreground and background color, whereas NLVS generates both false alarms and misses.

• **Comparison with semi-automatic method:** We compare our method with BSVS [29]. Since BSVS requires ground truth key frames, in this experiment we consider 3 different

configurations: Using 2 key frames, 6 key frames, and 10 key frames for each video sequence. This leads to 3 competing methods: BSVS2, BSVS6 and BSVS10. When testing, we feed the video sequence and the key frames to the algorithm. The output is a processed sequence, and the key frames are modified because the algorithm propagates the error.

The results of this experiment show that the proposed algorithm is better than BSVS even though BSVS has ground truth key frames. A visual comparison is shown in Figure 12.

• **Comparison with trimap + alpha-matting methods:** In this experiment we compare with a few alpha matting algorithms. The visual comparison is shown in Figure 14 and Figure 2, whereas the MAE value of DCNN [17] is shown in Figure 11.

The trimap + alpha-matting algorithm is substantially more robust against stationary objects where fully-automated background subtract methods failed. However, in order to make this method work, careful tuning during the trimap generation stage is required.

The results in Figure 14 and Figure 2 show that most alpha matting algorithms suffer from false alarms near the boundary, e.g., spectral matting [9], closed-form matting [20], learning-based matting [10] and comprehensive matting



[12]. The more recent methods such as K-nearest neighbors matting [11] and DCNN [13] have balanced errors in terms of false alarm and miss. Yet, the overall performance is still worse than the proposed method.

## 5 LIMITATIONS AND DISCUSSION

While the above experimental results demonstrate the superior performance of the proposed method, we should also highlight its limitations.

- **Quality of Plate Image.** The plate assumption may not hold when the background is moving substantially. When this happens, a more complex background model that includes dynamic information is needed. However, if the background is non-stationary, additional designs are needed to handle the local error and temporal consistency.
- **Loss of Fine Details.** In our proposed method, fine details such as hairs are compromised for robustness. Figure 15 illustrates an example. In some videos, the color difference between foreground and background is similar. This creates holes in the initial estimate  $r_0$ , can be filled by a strong denoiser such as total variation. However, total variation is known to oversmooth fine details. One alternative is to use sophisticated denoisers such as IrCNN (which produces better results as shown in Figure 8). However, IrCNN suffers from poor handling of the shadows.
- **Strong Shadows.** Strong shadows are sometimes treated as foreground, as shown in Figure 16. This is caused by the lack of shadow modeling in the problem formulation. The edge based initial estimate  $r_e$  can resolve the shadow issue to some extent, but not when the shadow is very strong. We tested a few off-the-shelf shadow removal algorithms [54]–[56], but generally they do not help because the shadow in our dataset can cast on the foreground object which should not be removed.

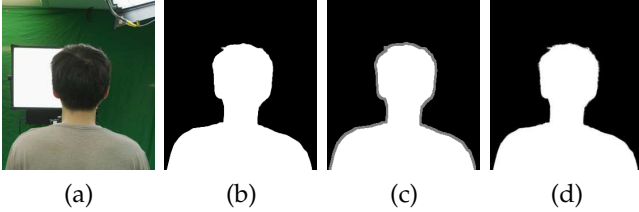


Fig. 15. Limitation 1: Loss of fine details. (a) Color input. (b) Our result. (c) Improving our result by generating a trimap from (b). (d) post-processed result by alpha matting using (b).



Fig. 16. Limitation 2: Strong shadows. When shadows are strong, they are easily misclassified as foreground.

## 6 CONCLUSION

This paper presents a new foreground extraction algorithm based on the multi-agent consensus equilibrium (MACE)

framework. MACE is an information fusion framework which integrates multiple weak experts to produce a strong estimator. Equipped with three customized agents: a dual-layer closed form matting agent, a background estimation agent and a total variation denoising agent, MACE offers substantially better foreground masks than state-of-the-art algorithms. MACE is a fully automatic algorithm, meaning that human interventions are not required. This provides significant advantage over semi-supervised methods which require trimaps or scribbles. In the current form, MACE is able to handle minor variations in the background plate image, illumination changes and weak shadows. Extreme cases can still cause MACE to fail, e.g., background movement or strong shadows. However, these could potentially be overcome by improving the background and shadow models.

## 7 APPENDIX

### 7.1 Proof of Theorem 1

*Proof.* There are two critical properties of  $\mathcal{G}$  to prove Theorem 1: (i)  $\mathcal{G}\mathcal{G} = \mathcal{G}$ , and (ii)  $(2\mathcal{G} - \mathcal{I})(2\mathcal{G} - \mathcal{I}) = \mathcal{I}$ .

To prove (i), we note that  $\mathcal{G}$  returns the average of the input and this averaging process is a projection. More precisely, we can show that

$$\mathcal{G}\mathcal{G}(\underline{v}^*) = \mathcal{G} \left( \begin{bmatrix} \langle \underline{v}^* \rangle \\ \vdots \\ \langle \underline{v}^* \rangle \end{bmatrix} \right) = \begin{bmatrix} \langle \underline{v}^* \rangle \\ \vdots \\ \langle \underline{v}^* \rangle \end{bmatrix} = \mathcal{G}(\underline{v}^*). \quad (41)$$

To prove (ii), we expand  $(2\mathcal{G} - \mathcal{I})(2\mathcal{G} - \mathcal{I})$  and show that

$$(2\mathcal{G} - \mathcal{I})(2\mathcal{G} - \mathcal{I}) = 4\mathcal{G}\mathcal{G} - 4\mathcal{G} + \mathcal{I} = 0, \quad (42)$$

where the last equality holds due to (i). In other words, (ii) shows that  $(2\mathcal{G} - \mathcal{I})$  is self-inverse.

Now we can prove Theorem 1. For notational simplicity we define  $\underline{x}^* \stackrel{\text{def}}{=} [\underline{x}^*; \dots; \underline{x}^*] \in \mathbb{R}^{nN}$ . Suppose  $(\underline{x}^*, \underline{u}^*)$  is the MACE solution. Then, (7) holds because  $\sum_{i=1}^N \underline{u}_i^* = 0$  by (6). For (8), we can show that

$$\begin{aligned} \mathcal{G}(\underline{v}^*) &= \mathcal{G}(\underline{x}^* + \underline{u}^*) \\ &= \begin{bmatrix} \frac{1}{N} \sum_{i=1}^N (\underline{x}^* + \underline{u}_i^*) \\ \vdots \\ \frac{1}{N} \sum_{i=1}^N (\underline{x}^* + \underline{u}_i^*) \end{bmatrix} = \begin{bmatrix} \underline{x}^* \\ \vdots \\ \underline{x}^* \end{bmatrix} \stackrel{\text{def}}{=} \underline{x}^*, \end{aligned} \quad (43)$$

On the other hand, since  $(\underline{x}^*, \underline{u}^*)$  satisfies (6), it holds that

$$\mathcal{F}(\underline{v}^*) = \mathcal{F}(\underline{x}^* + \underline{u}^*) = \underline{x}^*. \quad (44)$$

Therefore, we have  $\mathcal{F}(\underline{v}^*) = \mathcal{G}(\underline{v}^*)$ , and hence  $(2\mathcal{F} - \mathcal{I})(\underline{v}^*) = (2\mathcal{G} - \mathcal{I})(\underline{v}^*)$ . Since  $(2\mathcal{G} - \mathcal{I})$  is self-inverse, we show (8).

Conversely, if there exists a  $\underline{v}^*$  satisfying (7) and (8), then reversing the above steps we show  $\mathcal{F}(\underline{v}^*) = \mathcal{G}(\underline{v}^*)$ . Define  $\underline{x}^* = \frac{1}{N} \sum_{i=1}^N \underline{v}_i^*$  and  $\underline{u}^* = \underline{v}^* - \underline{x}^*$ . Then, we show that

$$\sum_{i=1}^N \underline{u}_i^* = \sum_{i=1}^N (\underline{v}_i^* - \underline{x}^*) = N\underline{x}^* - N\underline{x}^* = 0,$$

and

$$\mathcal{F}(\underline{x}^* + \underline{u}^*) = \mathcal{F}(\underline{v}^*) = \mathcal{G}(\underline{v}^*) = \underline{x}^*.$$

□

## 7.2 Proof of Theorem 2

*Proof.* We start by writing (19) in the matrix form

$$\tilde{J}(\alpha^I, \alpha^P, \mathbf{a}, \mathbf{b}) = \sum_{k \in I} \left\| \begin{bmatrix} \mathbf{H}_k & \mathbf{1} \\ \sqrt{\eta} \mathbf{G}_k & \sqrt{\eta} \mathbf{1} \\ \sqrt{\epsilon} \mathbf{I}_{3 \times 3} & \mathbf{0} \end{bmatrix} \begin{bmatrix} \mathbf{a}_k \\ b_k \end{bmatrix} - \begin{bmatrix} \alpha_k^I \\ \alpha_k^P \\ \mathbf{0} \end{bmatrix} \right\|^2$$

where

$$\mathbf{H}_k = \begin{bmatrix} \vdots & \vdots & \vdots \\ I_i^r & I_i^g & I_i^b \\ \vdots & \vdots & \vdots \end{bmatrix}, \quad \mathbf{G}_k = \begin{bmatrix} \vdots & \vdots & \vdots \\ P_i^r & P_i^g & P_i^b \\ \vdots & \vdots & \vdots \end{bmatrix},$$

$$\mathbf{a}_k = \begin{bmatrix} a_k^r \\ a_k^g \\ a_k^b \end{bmatrix}, \quad \alpha_k^I = \begin{bmatrix} \vdots \\ \alpha_k^I \\ \vdots \end{bmatrix}, \quad \alpha_k^P = \begin{bmatrix} \vdots \\ \alpha_k^P \\ \vdots \end{bmatrix},$$

and  $i$  denotes the index of the  $i$ -th pixel in the neighborhood  $w_k$ . The difference with the classic closed-form matting [20] is the new terms  $\mathbf{G}_k$ ,  $\mathbf{1}$  and  $\alpha_k^P$  (i.e., the second row of the quadratic function above.)

Denote

$$\mathbf{B}_k \stackrel{\text{def}}{=} \begin{bmatrix} \mathbf{H}_k & \mathbf{1} \\ \sqrt{\eta} \mathbf{G}_k & \sqrt{\eta} \mathbf{1} \\ \sqrt{\epsilon} \mathbf{I}_{3 \times 3} & \mathbf{0} \end{bmatrix}, \quad (45)$$

and use the fact that  $\alpha^P = \mathbf{0}$ , we can find out the solution of the least-squares optimization:

$$\begin{bmatrix} \mathbf{a}_k \\ b_k \end{bmatrix} = (\mathbf{B}_k^T \mathbf{B}_k)^{-1} \mathbf{B}_k^T \begin{bmatrix} \alpha_k^I \\ \mathbf{0} \\ \mathbf{0} \end{bmatrix} \quad (46)$$

We now need to simplify the term  $\mathbf{B}_k^T \mathbf{B}_k$ . First, observe that

$$\begin{aligned} \mathbf{B}_k^T \mathbf{B}_k &= \begin{bmatrix} \mathbf{H}_k^T \mathbf{H}_k + \eta \mathbf{G}_k^T \mathbf{G}_k + \epsilon \mathbf{I}_{3 \times 3} & \mathbf{H}_k^T \mathbf{1} + \eta \mathbf{G}_k^T \mathbf{1} \\ (\mathbf{H}_k \mathbf{1} + \eta \mathbf{G}_k \mathbf{1})^T & n(1 + \eta) \end{bmatrix} \\ &= \begin{bmatrix} \Sigma_k & \mu_k \\ \mu_k^T & c \end{bmatrix} \end{aligned}$$

where we define the terms  $\Sigma_k \stackrel{\text{def}}{=} \mathbf{H}_k^T \mathbf{H}_k + \eta \mathbf{G}_k^T \mathbf{G}_k + \epsilon \mathbf{I}$ ,  $\mu_k \stackrel{\text{def}}{=} \mathbf{H}_k^T \mathbf{1} + \eta \mathbf{G}_k^T \mathbf{1}$  and  $c \stackrel{\text{def}}{=} n(1 + \eta)$ . Then, by applying the block inverse identity, we have

$$(\mathbf{B}_k^T \mathbf{B}_k)^{-1} = \begin{bmatrix} \mathbf{T}_k^{-1} & -\mathbf{T}_k^{-1} \hat{\mu}_k \\ -(\mathbf{T}_k^{-1} \hat{\mu}_k)^T & \frac{1}{c} + \hat{\mu}_k^T \mathbf{T}_k^{-1} \hat{\mu}_k \end{bmatrix} \quad (47)$$

where we further define  $\mathbf{T}_k = \Sigma_k - \frac{\mu_k \mu_k^T}{c}$  and  $\hat{\mu}_k = \frac{\mu_k}{c}$ .

Substituting (46) back to  $\tilde{J}$ , and using (47), we have

$$\begin{aligned} \tilde{J}(\alpha^I) &= \sum_k \left\| (\mathbf{I}_{3 \times 3} - \mathbf{B}_k (\mathbf{B}_k^T \mathbf{B}_k)^{-1} \mathbf{B}_k^T) \begin{bmatrix} \alpha_k^I \\ \mathbf{0} \\ \mathbf{0} \end{bmatrix} \right\|^2 \\ &= (\alpha_k^I)^T \mathbf{L}_k \alpha_k^I, \end{aligned}$$

where

$$\begin{aligned} \mathbf{L}_k &= \mathbf{I}_{3 \times 3} - \left( \mathbf{H}_k \mathbf{T}_k^{-1} \mathbf{H}_k^T - \mathbf{H}_k \mathbf{T}_k^{-1} \hat{\mu}_k \mathbf{1}^T \right. \\ &\quad \left. - \mathbf{1}^T (\mathbf{T}_k^{-1} \hat{\mu}_k)^T \mathbf{H}_k + \frac{1}{c} \mathbf{1}^T \hat{\mu}_k \mathbf{T}_k^{-1} \hat{\mu}_k \mathbf{1} \right) \end{aligned} \quad (48)$$

The  $(i, j)$ -th element of  $\mathbf{L}_k$  is therefore

$$\begin{aligned} \mathbf{L}_k(i, j) &= \delta_{ij} - (\mathbf{I}_{ki}^T \mathbf{T}_k^{-1} \mathbf{I}_{kj} - \mathbf{I}_{ki}^T \mathbf{T}_k^{-1} \hat{\mu}_k \\ &\quad - \hat{\mu}_k^T \mathbf{T}_k^{-1} \mathbf{I}_{kj} + \frac{1}{c} + \hat{\mu}_k^T \mathbf{T}_k^{-1} \hat{\mu}_k) \\ &= \delta_{ij} - \left( \frac{1}{c} + (\mathbf{I}_{ki} - \hat{\mu}_k)^T \mathbf{T}_k^{-1} (\mathbf{I}_{kj} - \hat{\mu}_k) \right) \end{aligned} \quad (49)$$

Adding terms in each  $w_k$ , we finally obtain

$$\tilde{L}_{i,j} = \sum_{k | (i,j) \in w_k} \left\{ \delta_{ij} - \left( \frac{1}{c} + (\mathbf{I}_{ki} - \hat{\mu}_k)^T \mathbf{T}_k^{-1} (\mathbf{I}_{kj} - \hat{\mu}_k) \right) \right\}.$$

□

## 7.3 Proof: $\tilde{L}$ is positive definite

*Proof.* Recall the definition of  $\tilde{J}(\alpha^I, \alpha^P, \mathbf{a}, \mathbf{b})$ :

$$\begin{aligned} \tilde{J}(\alpha^I, \alpha^P, \mathbf{a}, \mathbf{b}) &= \sum_{j \in I} \left\{ \sum_{i \in w_j} \left( \alpha_i^I - \sum_c a_j^c I_i^c - b_j \right)^2 \right. \\ &\quad \left. + \eta \sum_{i \in w_j} \left( \alpha_i^P - \sum_c a_j^c P_i^c - b_j \right)^2 + \epsilon \sum_c (a_j^c)^2 \right\} \end{aligned}$$

Based on Theorem 2 we have,

$$\tilde{J}(\alpha) \stackrel{\text{def}}{=} \min_{\mathbf{a}, \mathbf{b}} \tilde{J}(\alpha, \mathbf{0}, \mathbf{a}, \mathbf{b}) = \alpha^T \tilde{L} \alpha. \quad (50)$$

We consider two cases: (i)  $a_j^c = 0 \forall j$  and  $\forall c$ , (ii) there exists some  $j$  and  $c$  such that  $a_j^c \neq 0$ . For the second case,  $\tilde{J}$  is larger than 0. For the first case,  $\tilde{J}$  can be reduced into

$$\tilde{J}(\alpha, \mathbf{0}, \mathbf{a}, \mathbf{b}) = \sum_{j \in I} \left\{ \sum_{i \in w_j} \left( (\alpha_i - b_j)^2 + \eta (-b_j)^2 \right) \right\} \quad (51)$$

For any vector  $\alpha \neq \mathbf{0}$ , there exists at least one  $\alpha_i \neq 0$ . Then by completing squares we can show that

$$\begin{aligned} &(\alpha_i - b_j)^2 + \eta b_j^2 \\ &= \alpha_i^2 - 2\alpha_i b_j + (1 + \eta) b_j^2 \\ &= \left( \sqrt{\frac{1}{1 + \eta}} \alpha_i - \sqrt{1 + \eta} b_j \right)^2 + \frac{\eta}{1 + \eta} \alpha_i^2 > 0 \end{aligned}$$

Therefore,  $\tilde{J}(\alpha, \mathbf{0}, \mathbf{a}, \mathbf{b}) > 0$  for any non-zero vector  $\alpha$ . As a result,  $\tilde{J}(\alpha, \mathbf{0}, \mathbf{a}, \mathbf{b}) = \alpha^T \tilde{L} \alpha > 0$  for both cases, and  $\tilde{L}$  is positive definite. □

## 7.4 Proof of Lemma 1

*Proof.* Let  $\underline{\mathbf{x}} \in \mathbb{R}^{nN}$  and  $\underline{\mathbf{y}} \in \mathbb{R}^{nN}$  be two super-vectors.

(i). If the  $F_i$ 's are non-expansive, then

$$\begin{aligned} &\|\mathcal{F}(\underline{\mathbf{x}}) - \mathcal{F}(\underline{\mathbf{y}})\|^2 + \|\underline{\mathbf{x}} - \underline{\mathbf{y}} - (\mathcal{F}(\underline{\mathbf{x}}) - \mathcal{F}(\underline{\mathbf{y}}))\|^2 \\ &= \sum_{i=1}^N (\|F_i(\mathbf{x}_i) - F_i(\mathbf{x}_i)\|^2 + \|\mathbf{x}_i - \mathbf{y}_i - (F_i(\mathbf{x}_i) - F_i(\mathbf{y}_i))\|^2) \\ &\stackrel{(c)}{\leq} \sum_{i=1}^N \|\mathbf{x}_i - \mathbf{y}_i\|^2 = \|\underline{\mathbf{x}} - \underline{\mathbf{y}}\|^2 \end{aligned}$$

where (c) holds because each  $F_i$  is firmly non-expansive. As a result,  $\mathcal{F}$  is also firmly non-expansive.

(ii). To prove that  $\mathcal{G}$  is firmly non-expansive, we recall from Theorem 1 (42) that  $2\mathcal{G} - \mathcal{I}$  is self-inverse. Since  $\mathcal{G}$  is linear, it has a matrix representation. Thus,  $\|(2\mathcal{G} - \mathcal{I})\mathbf{x}\|^2 = \mathbf{x}^T(2\mathcal{G} - \mathcal{I})^T(2\mathcal{G} - \mathcal{I})\mathbf{x}$ . Because  $\mathcal{G}$  is an averaging operator, it has to be symmetric, and hence  $\mathcal{G}^T = \mathcal{G}$ . As a result, we have  $\|(2\mathcal{G} - \mathcal{I})\mathbf{x}\|^2 = \|\mathbf{x}\|^2$  for any  $\mathbf{x}$ , which implies non-expansiveness.

(iii). If  $\mathcal{F}$  and  $\mathcal{G}$  are both firmly non-expansive, we have

$$\begin{aligned} & \|(2\mathcal{G} - \mathcal{I})[(2\mathcal{F} - \mathcal{I})(\mathbf{x})] - (2\mathcal{G} - \mathcal{I})[(2\mathcal{F} - \mathcal{I})(\mathbf{y})]\|^2 \\ & \stackrel{(a)}{\leq} \|(2\mathcal{F} - \mathcal{I})(\mathbf{x}) - (2\mathcal{F} - \mathcal{I})(\mathbf{y})\|^2 \stackrel{(b)}{\leq} \|\mathbf{x} - \mathbf{y}\|^2 \end{aligned}$$

where (a) is true due to the firmly non-expansiveness of  $\mathcal{G}$  and (b) is true due to the non-expansiveness of  $\mathcal{G}$ . Thus,  $\mathcal{T} \stackrel{\text{def}}{=} (2\mathcal{G} - \mathcal{I})(2\mathcal{F} - \mathcal{I})$  is non-expansive. This result also implies convergence of the MACE algorithm, due to [39].  $\square$

## 7.5 Proof of Lemma 2

*Proof.* The  $F_i$ 's we use in this paper are all proximal maps, and hence they are firmly non-expansive [41]. More specifically,  $F_1(\boldsymbol{\alpha}) = \underset{\boldsymbol{\alpha}}{\operatorname{argmin}} (\lambda_1/2)\|\boldsymbol{\alpha} - \mathbf{z}\|^2 + \boldsymbol{\alpha}^T \tilde{\mathbf{L}} \boldsymbol{\alpha}$  as  $\tilde{\mathbf{D}} = (1/2)\mathbf{I}$ . Since  $\tilde{\mathbf{L}}$  is positive definite,  $F_1$  is a proximal map.  $F_2$  is a minimization of a strongly convex function regularized by the proximal term, and so it is a proximal map.  $F_3$  is a standard total variation, and so it is a proximal map [57].  $\square$

## REFERENCES

- [1] M. Zyda, "From visual simulation to virtual reality to games," *Computer*, vol. 38, no. 9, pp. 25–32, Sep. 2005.
- [2] F. Biocca and M. R. Levy, Eds., *Communication in the age of virtual reality*, Routledge, Feb. 2013.
- [3] G. C. Burdea and P. Coiffet, *Virtual reality technology*, vol. 1, John Wiley & Sons, Jun. 2003.
- [4] R. P. McMahan, D. A. Bowman, D. J. Zielinski, and R. B. Brady, "Evaluating display fidelity and interaction fidelity in a virtual reality game," *IEEE Trans. on Visualization and Computer Graphics*, vol. 18, no. 4, pp. 626–633, Apr. 2012.
- [5] J. Chen, D. Bautembach, and S. Izadi, "Scalable real-time volumetric surface reconstruction," *ACM Trans. on Graphics (ToG)*, vol. 32, no. 4, Jul 2013, Article 113.
- [6] C. Rother, V. Kolmogorov, and A. Blake, "Grabcut: Interactive foreground extraction using iterated graph cuts," *ACM Trans. on Graphics (ToG)*, vol. 23, no. 3, pp. 309–314, Aug. 2004.
- [7] L. Wang, C. Zhang, R. Yang, and C. Zhang, "ToFCut: Towards robust real-time foreground extraction using a time-of-flight camera," in *Proc. of 3DPVT*, 2010, pp. 1–8.
- [8] A. Vacavant, T. Chateau, A. Whilhelm, and L. Lequievre, "A benchmark dataset for outdoor foreground/background extraction," in *Proc. Asian Conference on Computer Vision (ACCV)*, Berlin, Heidelberg, Nov. 2012, pp. 291–300, Springer.
- [9] A. Levin, A. Rav-Acha, and D. Lischinski, "Spectral matting," *IEEE Trans. on Pattern Analysis and Machine Intelligence*, vol. 30, no. 10, pp. 1699–1712, Oct. 2008.
- [10] Y. Zheng and C. Kambhampettu, "Learning based digital matting," in *Proc. IEEE International Conference on Computer Vision (ICCV)*, Sep. 2009, pp. 889–896.
- [11] Q. Chen, D. Li, and C. Tang, "KNN matting," *IEEE Trans. on Pattern Analysis and Machine Intelligence*, vol. 35, no. 9, pp. 2175–2188, Sep. 2013.
- [12] E. Shahrinan, D. Rajan, B. Price, and S. Cohen, "Improving image matting using comprehensive sampling sets," in *Proc. IEEE Conference on Computer Vision and Pattern Recognition (CVPR)*, Jun. 2013, pp. 636–643.
- [13] D. Cho, Y. Tai, and I. Kweon, "Natural image matting using deep convolutional neural networks," in *Proc. European Conference on Computer Vision (ECCV)*, Oct. 2016, pp. 626–643, Springer.
- [14] C. Hsieh and M. Lee, "Automatic trimap generation for digital image matting," in *Proc. IEEE Signal and Information Processing Association Annual Summit and Conference (APSIPA)*, Oct. 2013, pp. 1–5.
- [15] A. Al-Kabbany and E. Dubois, "A novel framework for automatic trimap generation using the gestalt laws of grouping," *Visual Information Processing and Communication VI*, vol. 9410, Mar. 2015, Article 94100G.
- [16] K. Lee, *Learning-based trimap generation for video matting*, Ph.D. thesis, University of California, San Diego, 2010.
- [17] D. Cho, S. Kim, and Y. W. Tai, "Automatic trimap generation and consistent matting for light-field images," *IEEE Trans. on Pattern Analysis and Machine Intelligence*, vol. 39, no. 8, pp. 1504–1517, Aug. 2017.
- [18] M. Camplani, L. Maddalena, G. M. Alcover, A. Petrosino, and L. Salgado, "A benchmarking framework for background subtraction in RGBD videos," in *New Trends in Image Analysis and Processing-ICIAP 2017 Workshops*, Sep. 2017, pp. 219–229, Springer.
- [19] M. Hofmann, P. Tiefenbacher, and G. Rigoll, "Background segmentation with feedback: The pixel-based adaptive segmenter," in *Proc. IEEE Conference on Computer Vision and Pattern Recognition Workshops (CVPRW)*, 2012, pp. 38–43.
- [20] A. Levin, D. Lischinski, and Y. Weiss, "A closed-form solution to natural image matting," *IEEE Trans. on Pattern Analysis and Machine Intelligence*, vol. 30, no. 2, pp. 228–242, Feb. 2008.
- [21] J. Sun, J. Jia, C. K. Tang, and H. Shum, "Poisson matting," *ACM Trans. on Graphics (ToG)*, vol. 23, no. 3, pp. 315–321, Aug. 2004.
- [22] E. Gastal and M. Oliveira, "Shared sampling for real-time alpha matting," *Euro Graphics*, vol. 29, no. 2, pp. 575–584, 2010.
- [23] Y. Y. Chuang, B. Curless, D. H. Salesin, and R. Szeliski, "A Bayesian approach to digital matting," in *Proc. IEEE Conference on Computer Vision and Pattern Recognition (CVPR)*, Dec 2001, vol. 2, pp. 11–18.
- [24] J. Wang and M. F. Cohen, "Optimized color sampling for robust matting," in *Proc. IEEE Conference on Computer Vision and Pattern Recognition (CVPR)*, Jun. 2007, pp. 1–8.
- [25] N. Xu, B. Price, and T. Huang, "Deep image matting," in *Proc. IEEE Conference on Computer Vision and Pattern Recognition (CVPR)*, Jul. 2017, pp. 311–320.
- [26] Y. Chuang, A. Agarwala, B. Curless, and D. H. Salesin, "Video matting of complex scenes," *ACM Trans. on Graphics (ToG)*, vol. 21, no. 3, pp. 243–248, Jul. 2002.
- [27] N. Apostoloff and A. Fitzgibbon, "Bayesian video matting using learnt image priors," in *Proc. IEEE Conference on Computer Vision and Pattern Recognition (CVPR)*, Jun. 2004, vol. 1, pp. 1–8.
- [28] S. Lee, J. Yoon, and I. Lee, "Temporally coherent video matting," *Graphical Models*, vol. 72, no. 3, pp. 25–33, May 2010.
- [29] N. Marki, F. Perazzi, O. Wang, and A. Sorkine-Hornung, "Bilateral space video segmentation," in *Proc. IEEE Conference on Computer Vision and Pattern Recognition (CVPR)*, 2016, pp. 743–751.
- [30] S. A. Ramakanth and R. V. Babu, "Seamseg: Video segmentation using patch seams," in *Proc. IEEE Conference on Computer Vision and Pattern Recognition (CVPR)*, Jun. 2014, vol. 2, pp. 376–383.
- [31] S. D. Jain and K. Grauman, "Supervoxel-consistent foreground propagation in video," in *Proc. European Conference on Computer Vision (ECCV)*, Sep. 2014, pp. 656–671, Springer.
- [32] Z. Zivkovic, "Improved adaptive gaussian mixture model for background subtraction," in *Proc. IEEE International Conference on Pattern Recognition*, Aug. 2004, vol. 2, pp. 28–31.
- [33] J. W. Davis and V. Sharma, "Fusion-based background-subtraction using contour saliency," in *Proc. IEEE Conference on Computer Vision and Pattern Recognition (CVPR)*, Jun. 2005, pp. 11–19.
- [34] V. Mahadevan and N. Vasconcelos, "Background subtraction in highly dynamic scenes," in *Proc. IEEE Conference on Computer Vision and Pattern Recognition (CVPR)*, Jun 2008, pp. 1–6.
- [35] J. Cho, T. Yamasaki, K. Aizawa, and K. H. Lee, "Depth video camera based temporal alpha matting for natural 3d scene generation," in *3DTV Conference: The True Vision-Capture, Transmission and Display of 3D Video (3DTV-CON)*, May 2011, pp. 1–4.
- [36] O. Wang, J. Finger, Q. Yang, J. Davis, and R. Yang, "Automatic natural video matting with depth," in *15th Pacific Conference On Computer Graphics and Applications*, Oct. 2007, pp. 469–472.

- [37] S. Sreehari, S. V. Venkatakrishnan, B. Wohlberg, G. T. Buzzard, L. F. Drummy, J. P. Simmons, and C. A. Bouman, "Plug-and-play priors for bright field electron tomography and sparse interpolation," *IEEE Trans. on Computational Imaging*, vol. 2, no. 4, pp. 408–423, Dec. 2016.
- [38] S. H. Chan, X. Wang, and O. A. Elgandy, "Plug-and-play ADMM for image restoration," *IEEE Trans. on Computational Imaging*, vol. 3, no. 1, pp. 84–98, Mar. 2017.
- [39] G. Buzzard, S. H. Chan, S. Sreehari, and C. A. Bouman, "Plug-and-play unplugged: optimization free reconstruction using consensus equilibrium," accepted to SIAM J. Imaging Sciences. Available online <http://arxiv.org/abs/1705.08983>, 2017.
- [40] S. Boyd, N. Parikh, E. Chu, B. Peleato, and J. Eckstein, "Distributed optimization and statistical learning via the alternating direction method of multipliers," *Foundations and Trends in Machine learning*, vol. 3, no. 1, pp. 1–22, Jul. 2011.
- [41] N. Parikh and S. Boyd, "Proximal algorithms," *Foundations and Trends in Optimization*, vol. 1, no. 3, pp. 127–239, Jan. 2014.
- [42] S. Venkatakrishnan, C. Bouman, and B. Wohlberg, "Plug-and-play priors for model based reconstruction," in *Proc. IEEE Global Conference on Signal and Information Processing*, Dec. 2013, pp. 945–948.
- [43] X. Wang and S. H. Chan, "Parameter-free-plug-and-play ADMM for image restoration," in *Proc. IEEE International Conference on Acoustic, Speech, Signal Process. (ICASSP)*, Mar. 2017, pp. 1323–1327.
- [44] S. V. Burtsev and Y. P. Kuzmin, "An efficient flood-fill algorithm," *Computers & Graphics*, vol. 17, no. 5, pp. 549–561, Sept 1993.
- [45] S. H. Chan, R. Khoshabeh, K. B. Gibson, P. E. Gill, and T. Q. Nguyen, "An augmented Lagrangian method for total variation video restoration," *IEEE Trans. on Image Processing*, vol. 20, no. 11, pp. 3097–3111, May 2011.
- [46] K. Dabov, A. Foi, V. Katkovnik, and K. Egiazarian, "Image denoising by sparse 3D transform-domain collaborative filtering," *IEEE Trans. on Image Processing*, vol. 16, no. 8, pp. 2080–2095, Aug. 2007.
- [47] K. Zhang, W. Zuo, S. Gu, and L. Zhang, "Learning deep cnn denoiser for image restoration," in *Proc. IEEE Conference on Computer Vision and Pattern Recognition (CVPR)*, Jul. 2017, pp. 2808–2817.
- [48] K. Toyama, J. Krumm, B. Brumitt, and M. B. Wallflower, "Principles and practice of background maintenance," in *Proc. IEEE International Conference on Computer Vision (ICCV)*, Sep. 1999, vol. 1, pp. 255–261.
- [49] L. Li, W. Huang, I. Y. H. Gu, and Q. Tian, "Statistical modeling of complex backgrounds for foreground object detection," *IEEE Trans. on Image Processing*, vol. 13, no. 11, pp. 1459–1472, Nov. 2004.
- [50] Y. Sheikh and M. Shah, "Bayesian modeling of dynamic scenes for object detection," *IEEE Trans. on Pattern Analysis and Machine Intelligence*, vol. 27, no. 11, pp. 1778–1792, Nov. 2005.
- [51] C. Benedek and T. Sziranyi, "Bayesian foreground and shadow detection in uncertain frame rate surveillance videos," *IEEE Trans. on Image Processing*, vol. 17, no. 4, pp. 608–621, Apr. 2008.
- [52] O. Barnich and V. D. Marc, "ViBe: A universal background subtraction algorithm for video sequences," *IEEE Trans. on Image Processing*, vol. 20, no. 6, pp. 1709–1724, Jun. 2011.
- [53] A. Faktor and M. Irani, "Video segmentation by non-local consensus voting," in *Proc. British Machine Vision Association (BMVC)*, Jun. 2014, vol. 2, p. 8.
- [54] R. Guo, Q. Dai, and D. Hoiem, "Single-image shadow detection and removal using paired regions," in *proc. IEEE Conference on Computer Vision and Pattern Recognition (CVPR)*, Jun. 2011, pp. 2033–2040.
- [55] E. Arbel and H. Hel-Or, "Shadow removal using intensity surfaces and texture anchor points," *IEEE Trans. on Pattern Analysis and Machine Intelligence*, vol. 33, no. 6, pp. 1202–1216, Jun. 2011.
- [56] F. Liu and M. Gleicher, "Texture-consistent shadow removal," in *Proc. European Conference on Computer Vision (ECCV)*, Oct. 2008, pp. 437–450, Springer.
- [57] H. H. Bauschke, "New demiclosedness principles for (firmly) non-expansive operators," *Computational and Analytical Mathematics*, pp. 19–28, 2013.



# Automatic Foreground Extraction using Multi-Agent Consensus Equilibrium (Supplementary Material)

Xiran Wang, *Student Member, IEEE*, Jason Juang and Stanley H. Chan, *Senior Member, IEEE*

This Supplementary Report provides additional experimental results of the MACE algorithm.

## I. ADDITIONAL COMPARISON WITH ALPHA MATTING ALGORITHMS

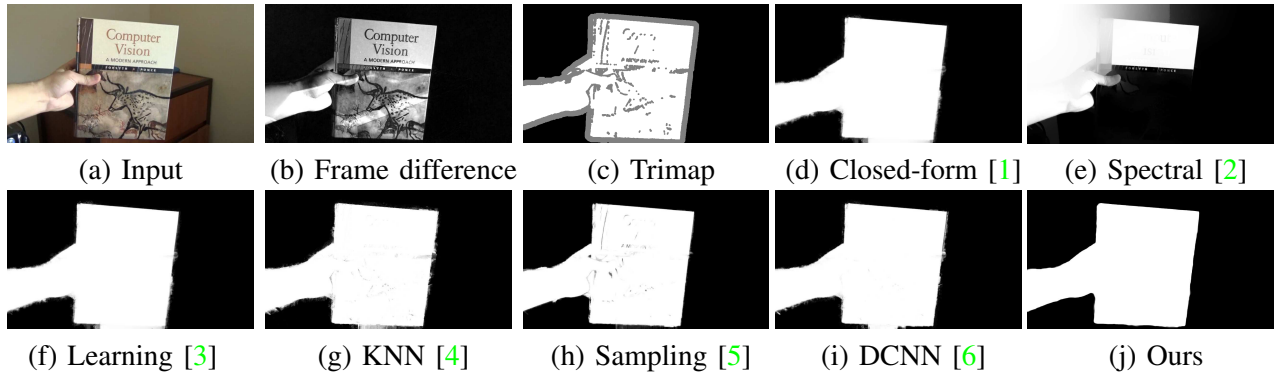


Fig. 1. Comparison with alpha-matting algorithms. (a) Input image. (b) Binary mask returned by the standard background subtraction algorithm in OpenCV. (c) Trimap generated by morphographic operation (dilation / erosion) of the binary mask. (d) - (i) Alpha matting algorithms available on [alphamatting.com](http://alphamatting.com). (j) Proposed method.

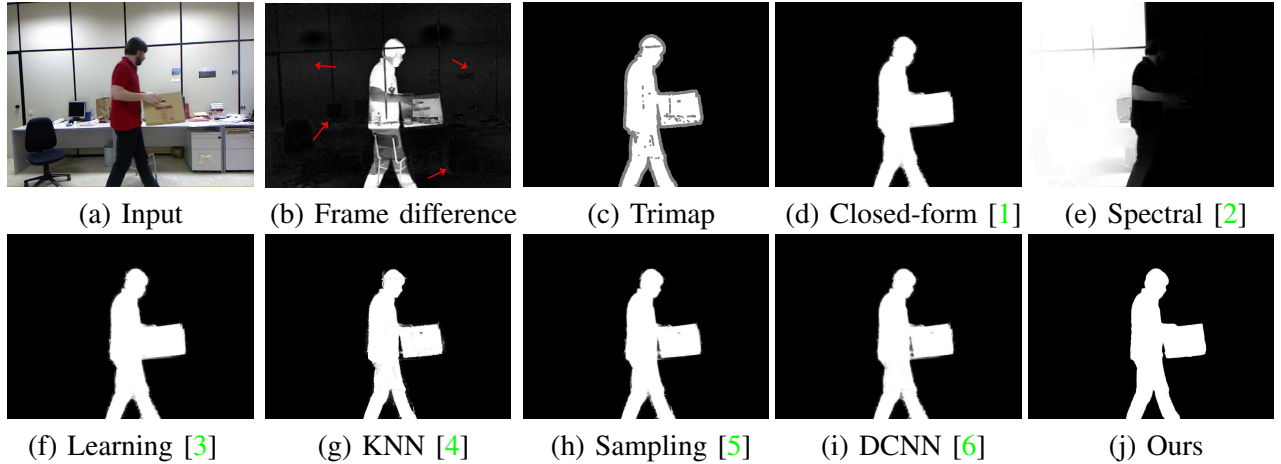


Fig. 2. Comparison with alpha-matting algorithms. (a) Input image. (b) Binary mask returned by the standard background subtraction algorithm in OpenCV. (c) Trimap generated by morphographic operation (dilation / erosion) of the binary mask. (d) - (i) Alpha matting algorithms available on [alphamatting.com](http://alphamatting.com). (j) Proposed method.

X. Wang and S. Chan are with the School of Electrical and Computer Engineering, Purdue University, West Lafayette, IN 47907, USA. Email: { wang470, stanchan}@purdue.edu.

J. Juang is with HypeVR Inc., San Diego, CA 92108, USA. Email: [jason@hypevr.com](mailto:jason@hypevr.com)

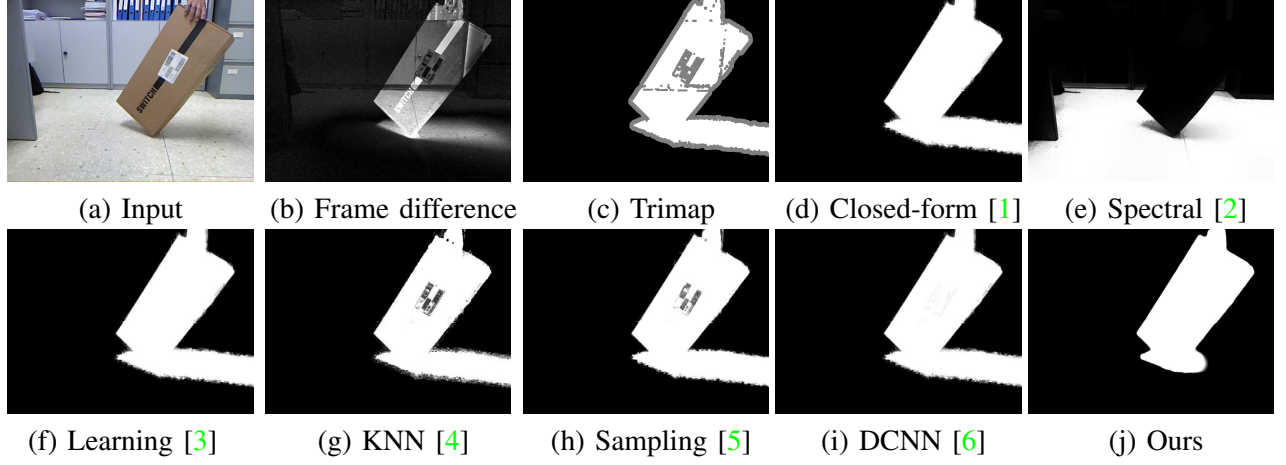


Fig. 3. Comparison with alpha-matting algorithms. (a) Input image. (b) Binary mask returned by the standard background subtraction algorithm in OpenCV. (c) Trimap generated by morphographic operation (dilation / erosion) of the binary mask. (d) - (i) Alpha matting algorithms available on [alphamatting.com](http://alphamatting.com). (j) Proposed method.

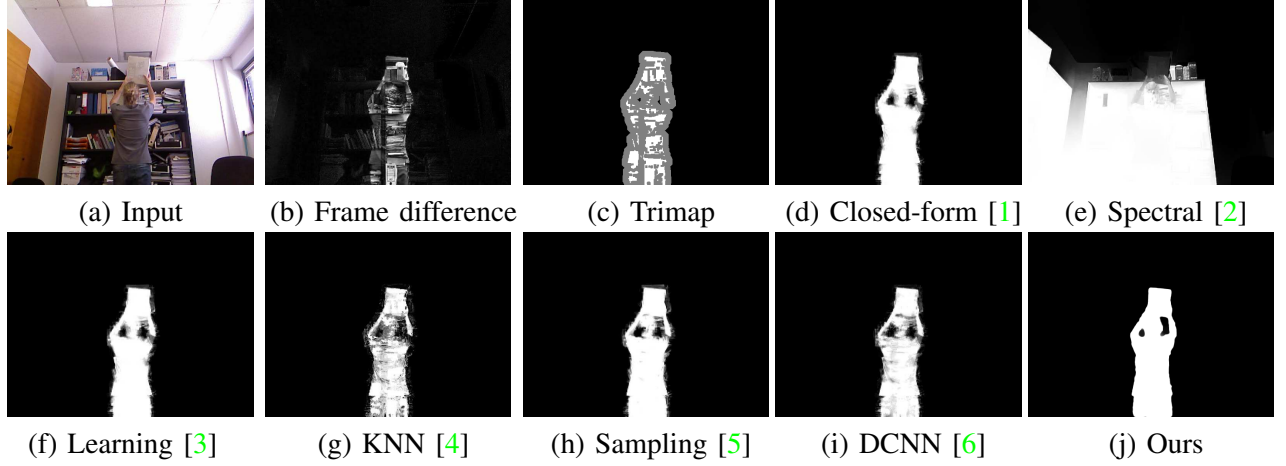


Fig. 4. Comparison with alpha-matting algorithms. (a) Input image. (b) Binary mask returned by the standard background subtraction algorithm in OpenCV. (c) Trimap generated by morphographic operation (dilation / erosion) of the binary mask. (d) - (i) Alpha matting algorithms available on [alphamatting.com](http://alphamatting.com). (j) Proposed method.

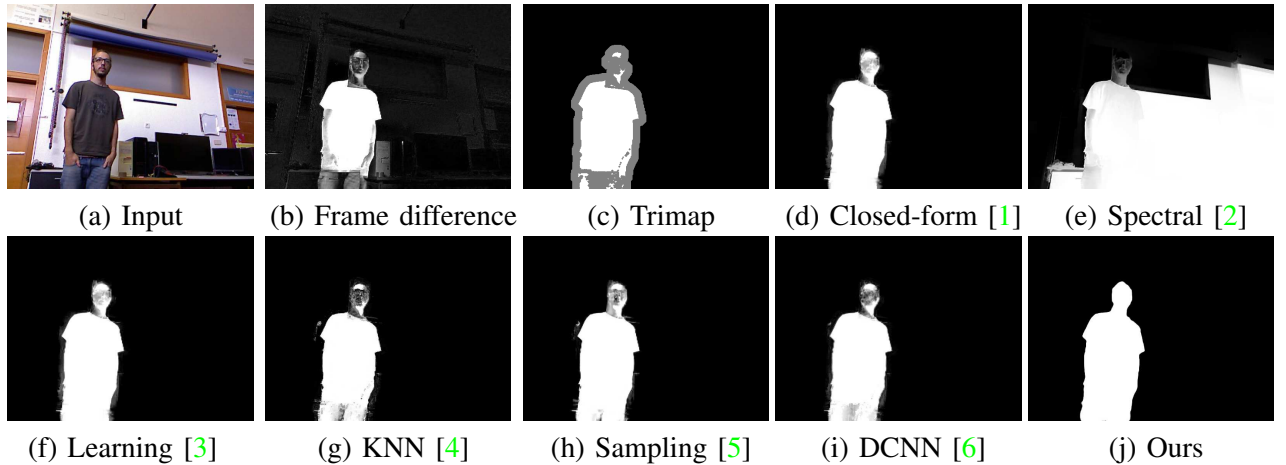


Fig. 5. Comparison with alpha-matting algorithms. (a) Input image. (b) Binary mask returned by the standard background subtraction algorithm in OpenCV. (c) Trimap generated by morphographic operation (dilation / erosion) of the binary mask. (d) - (i) Alpha matting algorithms available on [alphamatting.com](http://alphamatting.com). (j) Proposed method.

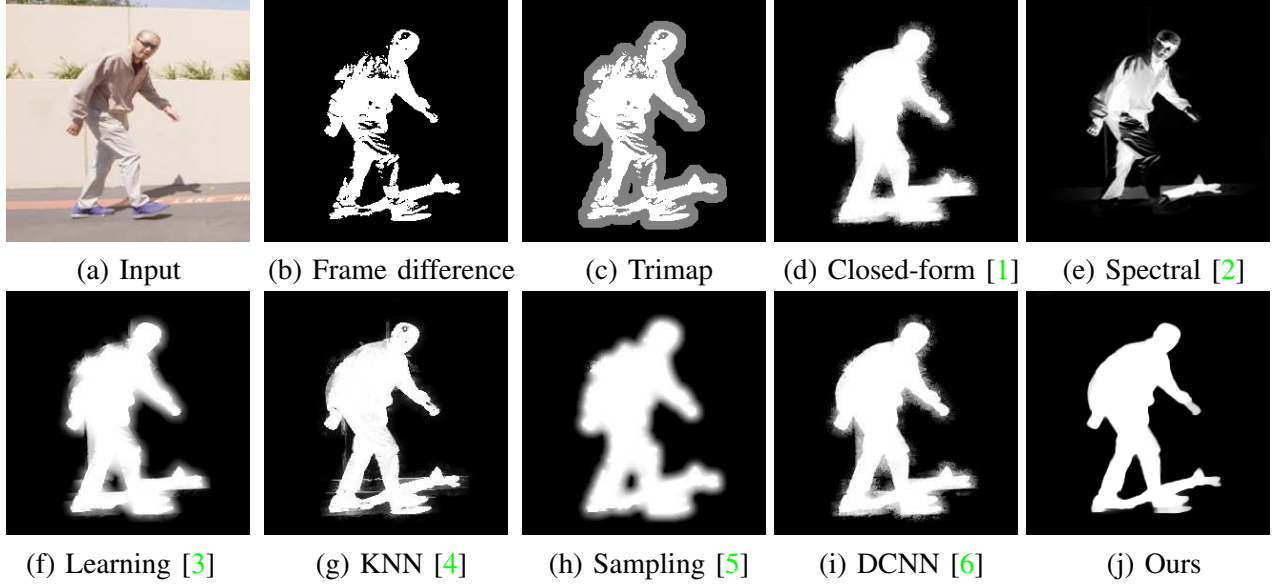


Fig. 6. Comparison with alpha-matting algorithms. (a) Input image. (b) Binary mask returned by the standard background subtraction algorithm in OpenCV. (c) Trimap generated by morphographic operation (dilation / erosion) of the binary mask. (d) - (i) Alpha matting algorithms available on [alphamatting.com](http://alphamatting.com). (j) Proposed method.



Fig. 7. Road sequence results. (a) Input. (b) Ground truth. (c) PBAS [7]. (d) ViBe [8]. (e) BSVS [9]. (f) NLVS [10]. (g) Ours.

## II. NUMERICAL VALUES OF FALSE ALARMS AND MISSES

The following two tables show the detailed values of False Alarm and Miss.

### A. Comparison with Fully-automated Methods.

	PBAS			ViBe			NLVS			Trimap			Proposed		
Video	FA	Miss	MAE	FA	Miss	MAE	FA	Miss	MAE	FA	Miss	MAE			
Book	0.0056	0.1551	0.1606	0.0124	0.1070	0.1194	0.0004	0.0252	0.0255	0.0035	0.0011	0.0046	0.0018	0.0004	<b>0.0022</b>
Building	0.0033	0.0023	0.0056	0.0038	0.0034	0.0072	0.0002	0.0033	0.0034	0.0010	0.0027	0.0037	0.0023	0.0001	<b>0.0024</b>
Coach	0.0083	0.0331	0.0413	0.0115	0.0076	0.0192	0.0245	0.0431	0.0677	0.0190	0.0014	0.0204	0.0006	0.0010	<b>0.0016</b>
Studio	0.0441	0.4881	0.5322	0.0019	0.2358	0.2377	0.0109	0.4652	0.4761	0.0041	0.0003	0.0044	0.0019	0.0002	<b>0.0021</b>
Road	0.0032	0.0017	0.0049	0.0043	0.0021	0.0063	0.0002	0.0027	0.0029	0.0021	0.0004	0.0025	0.0004	0.0000	<b>0.0004</b>
Tackle	0.0040	0.0081	0.0121	0.0024	0.0014	0.0039	0.0020	0.0071	0.0090	0.0059	0.0000	0.0059	0.0013	0.0001	<b>0.0013</b>
Gravel	0.0005	0.0060	0.0065	0.0008	0.0074	0.0082	0.0001	0.0048	0.0049	0.0024	0.0003	0.0027	0.0003	0.0006	<b>0.0009</b>
Office	0.0021	0.0092	0.0113	0.0007	0.0073	0.0080	0.0005	0.0086	0.0092	0.0058	0.0008	0.0066	0.0011	0.0000	<b>0.0011</b>
Bootstrap	0.0995	0.0976	0.1971	0.0251	0.0883	0.1135	0.0013	0.0541	0.0555	0.0061	0.0015	0.0076	0.0028	0.0006	<b>0.0034</b>
Cespatx	0.0022	0.0488	0.0510	0.0029	0.0330	0.0359	0.0032	0.0473	0.0505	0.0243	0.0005	0.0248	0.0036	0.0018	<b>0.0054</b>
DCam	0.0023	0.0443	0.0467	0.0034	0.0201	0.0236	0.0003	0.0328	0.0331	0.0474	0.0010	0.0484	0.0051	0.0033	<b>0.0084</b>
Gen	0.0095	0.0143	0.0238	0.0128	0.0071	0.0200	0.0005	0.0153	0.0158	0.0243	0.0002	0.0245	0.0079	0.0004	<b>0.0084</b>
Multipeople	0.0259	0.0050	0.0308	0.0602	0.0062	0.0664	0.0076	0.0253	0.0329	0.0140	0.0012	0.0152	0.0068	0.0010	<b>0.0078</b>
Shadow	0.0072	0.0279	0.0351	0.0310	0.0075	0.0385	0.0005	0.0270	0.0275	0.0247	0.0106	0.0353	0.0098	0.0001	<b>0.0098</b>
Avg	0.0156	0.0673	0.0828	0.0124	0.0382	0.0506	0.0037	0.0544	0.0581	0.0132	0.0016	0.0148	0.0033	0.0007	<b>0.0039</b>

TABLE I

COMPARISON OF FULLY-AUTOMATED METHODS IN TERMS OF FALSE ALARM (FA), MISS (MISS) AND TOTAL MAE, WHERE MAE = FA + MISS. LOWER IS BETTER.

### B. Comparison with Semi-automated Methods.

	BSVS(2)			BSVS(6)			BSVS(10)			Proposed		
Video	FA	Miss	MAE	FA	Miss	MAE	FA	Miss	MAE	FA	Miss	MAE
Book	0.0014	0.1054	0.1068	0.0067	0.0115	0.0182	0.0014	0.0105	0.0119	0.0018	0.0004	<b>0.0022</b>
Building	0.0002	0.0069	0.0071	0.0002	0.0033	0.0035	0.0002	0.0026	0.0028	0.0023	0.0001	<b>0.0024</b>
Coach	0.0006	0.0011	0.0017	0.0005	0.0010	0.0015	0.0004	0.0009	<b>0.0013</b>	0.0006	0.0010	0.0016
Studio	0.0020	0.0004	0.0024	0.0014	0.0004	0.0018	0.0013	0.0004	<b>0.0017</b>	0.0019	0.0002	0.0021
Road	0.0003	0.0061	0.0064	0.0002	0.0026	0.0028	0.0001	0.0010	0.0011	0.0004	0.0000	<b>0.0004</b>
Tackle	0.0016	0.0014	0.0030	0.0014	0.0005	0.0019	0.0013	0.0011	0.0025	0.0013	0.0001	<b>0.0013</b>
Gravel	0.0004	0.0128	0.0132	0.0002	0.0067	0.0069	0.0006	0.0041	0.0047	0.0003	0.0006	<b>0.0009</b>
Office	0.0003	0.0232	0.0235	0.0004	0.0100	0.0104	0.0007	0.0036	0.0044	0.0011	0.0000	<b>0.0011</b>
Bootstrap	0.0034	0.0094	0.0128	0.0043	0.0038	0.0080	0.0036	0.0038	0.0075	0.0028	0.0006	<b>0.0034</b>
Cespatx	0.0120	0.0545	0.0665	0.0118	0.0252	0.0370	0.0133	0.0140	0.0274	0.0036	0.0018	<b>0.0054</b>
DCam	0.0063	0.0351	0.0414	0.0090	0.0146	0.0236	0.0078	0.0091	0.0169	0.0051	0.0033	<b>0.0084</b>
Gen	0.0047	0.0198	0.0245	0.0052	0.0086	0.0139	0.0049	0.0071	0.0120	0.0079	0.0004	<b>0.0084</b>
Multipeople	0.0055	0.0158	0.0213	0.0038	0.0154	0.0192	0.0042	0.0083	0.0125	0.0068	0.0010	<b>0.0078</b>
Shadow	0.0019	0.0108	0.0126	0.0015	0.0040	0.0055	0.0013	0.0032	<b>0.0045</b>	0.0098	0.0001	0.0098
Avg	0.0029	0.0216	0.0245	0.0033	0.0077	0.0110	0.0029	0.0050	0.0079	0.0033	0.0007	<b>0.0039</b>

TABLE II

COMPARISON OF BSVS IN TERMS OF FALSE ALARM (FA), MISS (MISS) AND TOTAL MAE, WHERE MAE = FA + MISS. LOWER IS BETTER.

## REFERENCES

- [1] A. Levin, D. Lischinski, and Y. Weiss, "A closed-form solution to natural image matting," *IEEE Trans. on Pattern Analysis and Machine Intelligence*, vol. 30, no. 2, pp. 228–242, Feb. 2008. **1, 2, 3**
- [2] A. Levin, A. Rav-Acha, and D. Lischinski, "Spectral matting," *IEEE Trans. on Pattern Analysis and Machine Intelligence*, vol. 30, no. 10, pp. 1699–1712, Oct. 2008. **1, 2, 3**
- [3] Y. Zheng and C. Kambhampettu, "Learning based digital matting," in *Proc. IEEE International Conference on Computer Vision (ICCV)*, Sep. 2009, pp. 889–896. **1, 2, 3**
- [4] Q. Chen, D. Li, and C. Tang, "KNN matting," *IEEE Trans. on Pattern Analysis and Machine Intelligence*, vol. 35, no. 9, pp. 2175–2188, Sep. 2013. **1, 2, 3**



- [5] E. Shahrian, D. Rajan, B. Price, and S. Cohen, "Improving image matting using comprehensive sampling sets," in *Proc. IEEE Conference on Computer Vision and Pattern Recognition (CVPR)*, Jun. 2013, pp. 636–643. 1, 2, 3
- [6] D. Cho, Y. Tai, and I. Kweon, "Natural image matting using deep convolutional neural networks," in *Proc. European Conference on Computer Vision (ECCV)*. Oct. 2016, pp. 626–643, Springer. 1, 2, 3
- [7] M. Hofmann, P. Tiefenbacher, and G. Rigoll, "Background segmentation with feedback: The pixel-based adaptive segmenter," in *Proc. IEEE Conference on Computer Vision and Pattern Recognition Workshops (CVPRW)*, 2012, pp. 38–43. 3
- [8] O. Barnich and V. D. Marc, "ViBe: A universal background subtraction algorithm for video sequences," *IEEE Trans. on Image Processing*, vol. 20, no. 6, pp. 1709–1724, Jun. 2011. 3
- [9] N. Marki, F. Perazzi, O. Wang, and A. Sorkine-Hornung, "Bilateral space video segmentation," in *Proc. IEEE Conference on Computer Vision and Pattern Recognition (CVPR)*, 2016, pp. 743–751. 3
- [10] A. Faktor and M. Irani, "Video segmentation by non-local consensus voting," in *Proc. British Machine Vision Association (BMVC)*, Jun. 2014, vol. 2, p. 8. 3